Article

SOURCE DATA | TRANSPARENT PROCESS

THE EMBO JOURNAL

Human shelterin protein POT1 prevents severe telomere instability induced by homology-directed DNA repair

Galina Glousker[1,*], Anna-Sophia Briod[1], Manfredo Quadroni[2] & Joachim Lingner[1,**]

Abstract

The evolutionarily conserved POT1 protein binds single-stranded G-rich telomeric DNA and has been implicated in contributing to telomeric DNA maintenance and the suppression of DNA damage checkpoint signaling. Here, we explore human POT1 function through genetics and proteomics, discovering that a complete absence of POT1 leads to severe telomere maintenance defects that had not been anticipated from previous depletion studies in human cells. Conditional deletion of *POT1* in HEK293E cells gives rise to rapid telomere elongation and length heterogeneity, branched telomeric DNA structures, telomeric R-loops, and telomere fragility. We determine the telomeric proteome upon POT1-loss, implementing an improved telomeric chromatin isolation protocol. We identify a large set of proteins involved in nucleic acid metabolism that engage with telomeres upon POT1-loss. Inactivation of the homology-directed repair machinery suppresses POT1-loss-mediated telomeric DNA defects. Our results unravel as major function of human POT1 the suppression of telomere instability induced by homology-directed repair.

Keywords DNA damage response; homologous recombination; POT1; R-loops; telomeric proteome

Subject Categories Chromatin, Transcription & Genomics; DNA Replication, Recombination & Repair

DOI 10.15252/embj.2020104500 | Received 17 January 2020 | Revised 15 September 2020 | Accepted 18 September 2020 | Published online 19 October 2020

The EMBO Journal (2020) 39: e104500

Introduction

Telomeres, the nucleoprotein structures at chromosome ends, are distinct from chromosome internal breaks in remarkable ways. Telomeric proteins protect chromosome ends from degradation and suppress DNA damage signaling. In addition, they prevent DNA end-to-end fusions by non-homologous end joining and they suppress inter- and intra-chromosomal homologous recombination between telomere repeats, which can lead to rampant telomere elongation and loss events.

Many of the telomere functions are mediated by the shelterin proteins comprising TRF1, TRF2, RAP1, TIN2, TPP1, and POT1 which cover large parts of telomeric DNA (Lazzerini-Denchi & Sfeir, 2016; de Lange, 2018). POT1 is a highly conserved telomere-binding protein which binds the telomeric single-stranded G-rich DNA present as a 3′overhang at the end of the chromosomes (Baumann & Cech, 2001). Alternatively, when telomeres adopt a t-loop structure in which the single-stranded 3′ overhang is tucked into double-stranded part of the telomere (Doksani *et al*, 2013), POT1 is thought to bind to the single-stranded displaced G-rich strand. Though POT1 binds directly to the single-stranded telomeric DNA, it is recruited to telomeres through its physical interaction with the shelterin component TPP1 (Takai *et al*, 2011), which in turn interacts with TIN2 that is associated with the double strand telomere-binding proteins TRF1 and TRF2 (de Lange, 2018). This type of molecular architecture is similar from mammals to fission yeast suggesting widespread conservation in evolution (Miyoshi *et al*, 2008).

Studies in a variety of eukaryotes unraveled important functions of POT1 in chromosome end protection and telomere length control. In fission yeast, Pot1-loss leads to rapid loss of telomeric DNA and chromosome circularization suggesting roles in protecting chromosome ends from nucleolytic degradation (Baumann & Cech, 2001; Pitt & Cooper, 2010). In mammals, such dramatic telomere loss events are not seen upon depletion of POT1. In contrast to the human genome, the mouse genome contains two *POT1* paralogs, *Pot1a and Pot1b,* and studies in this organism have contributed to the understanding of POT1 function (Hockemeyer *et al*, 2006; Wu *et al*, 2006). Deletion of conditional alleles in mouse embryonic fibroblasts (MEFs) revealed that POT1a represses ATR signaling which is triggered through RPA binding to single-stranded telomeric DNA (Hockemeyer *et al*, 2006; Wu *et al*, 2006) whereas POT1b regulates the telomeric DNA overhang structure (Hockemeyer *et al*, 2006). *Pot1a* deletion in MEFs *per se* was also reported to increase homologous recombination (HR) in one study (Wu *et al*, 2006) but not the other (Hockemeyer *et al*, 2006). However, concomitant deletion of *Pot1a* and *Pot1b* induced higher incidences of telomere sister

1 School of Life Sciences, Swiss Institute for Experimental Cancer Research (ISREC), Ecole Polytechnique Fédérale de Lausanne (EPFL), Lausanne, Switzerland
2 Protein Analysis Facility, University of Lausanne, Lausanne, Switzerland
*Corresponding author. Tel: +41 216930723; E-mail: galina.glousker@epfl.ch
**Corresponding author. Tel: +41 216930721; E-mail: joachim.lingner@epfl.ch

© 2020 The Authors

chromatid exchanges in $Ku70^{-/-}$ cells suggesting contributions of mouse POT1a/b to the suppression of homology-directed repair (HDR) in $Ku70^{-/-}$ cells (Palm *et al*, 2009). The functions of POT1 in human cells had so far been mostly assessed by overexpression or RNAi-mediated depletion but not knockout studies. In addition to the telomeric DNA damage response, POT1 reduction induced incorrect 5′ end processing in which telomeres lost the preferred ending with ATC-5′ to random positions within the telomeric repeat sequence (Hockemeyer *et al*, 2005).

Several studies also suggest direct or indirect roles of POT1 in semiconservative DNA replication and in telomere length control by telomerase. Overexpression of POT1 mutants which are prevalent in T-cell lymphoma in human fibrosarcoma HT1080 cells increased telomere fragility which is indicative of DNA replication defects (Pinzaru *et al*, 2016). This effect was suspected to be due to defects of the POT1 mutants in POT1-assisted assembly of the CST complex (Pinzaru *et al*, 2016) which promotes lagging strand synthesis at telomeres. In addition, POT1 can regulate telomerase. Overexpression of a mutant form of human POT1 that lacks the DNA-binding OB-fold induces rapid telomere elongation (Loayza & De Lange, 2003; Zhong *et al*, 2012) and POT1 also inhibits telomerase *in vitro* (Kelleher *et al*, 2005). On the other hand, in conjunction with TPP1, POT1 can stimulate telomerase processivity *in vitro* (Latrick & Cech, 2010).

In this paper, we assess human POT1 function by analyzing the consequence of POT1 loss upon conditional deletion in HEK293E cells. We demonstrate that the complete absence of POT1 triggers telomeric DNA branching, telomere elongation, accumulation of G-rich telomeric DNA, telomeric R-loops, and telomere fragility. We elucidate changes in the telomeric proteome establishing an improved telomeric chromatin isolation protocol, identifying among others HDR factors that accumulate at telomeres in the absence of POT1. Significantly, the severe telomere maintenance defects but not the DNA damage response in the absence of POT1 are all suppressed upon inactivation of the HDR machinery. Thus, a major function of human POT1 is the repression of telomeric homologous recombination.

Results

POT1-loss triggers rapid telomere elongation and a DNA damage response throughout the cell cycle

In order to study the functions of human POT1 for the maintenance of telomeric DNA structure and telomeric protein composition, we genetically modified HEK293E cells. HEK293E cells were originally derived from a human embryonic kidney preparation but are presumably of adrenal origin (Lin *et al*, 2014). They contain the *E1A* adenovirus gene and *EBNA1* from Epstein–Barr virus. We first tagged using CRIPSR/Cas9 gene editing the *TRF1* and *TRF2* genes at their N-termini with triple FLAG-tags to facilitate isolation of telomere chromatin as explained below. Cell clones were isolated and genotyped by PCR. Addition of these tags in chosen clone 293E cl75 did not interfere with telomere maintenance as assessed by telomere restriction fragment length (TRF) analysis nor did it induce a telomeric DNA damage response. In a second step, we sought to develop a conditional allele of human *POT1* in 293E cl75, inserting by CRISPR/Cas9 gene editing LoxP sites in the introns flanking exon 6 (Fig 1A). We screened clonal isolates by PCR and sequencing for the appropriate genotype (Fig 1B, and Appendix Fig S1A and B). 293E cl75p100 carried two *POT1* alleles with the desired LoxP sites flanking exon 6 and a third allele with a frameshift mutation in exon 6 giving rise to a premature stop codon. Of note, HEK293E cells are triploid for chromosome 7, which harbors *POT1*. 293E cl75p100 maintains constant telomere length over several weeks of growth as assessed by TRF analysis (Appendix Fig S1C). We then transduced clone 293E cl75p100 with CreERT2 lentivirus expressing tamoxifen-dependent Cre recombinase to allow excision of the DNA between the LoxP sites. Cells were again cloned and screened for efficient editing of the conditional *POT1* alleles upon addition of 4-hydroxytamoxifen (4OHT) scoring for loss of POT1 protein expression by Western blot analysis (Appendix Fig S1D). Two clones (293E 75p100 Cre35 and 293E 75p100 Cre45) showed efficient loss of POT1 protein and induction of the DNA damage marker γ-H2AX as expected (Appendix Fig S1D). Phosphorylated forms of ATM and CHK1 also accumulated upon induced deletion of *POT1* (Fig 1C).

We assessed the effects of POT1-loss on telomeric DNA by TRF analysis of non-denatured DNA to detect single-stranded G-rich telomeric DNA and of denatured DNA to measure telomere length distribution (Fig 1D and Appendix Fig S1E). Very strikingly, loss of POT1 for more than 3–4 days caused dramatic telomere elongation, an increase of single-stranded G-rich telomeric DNA, and an accumulation of telomeric DNA molecules that could not enter the gel, suggestive of branched DNA structures. The viability and the proliferation of the cells upon POT1-loss were strongly affected after 4 days of culture in presence of 4OHT (Fig 1E). Analysis of cellular DNA content by fluorocytometry indicated that during the time course, the fraction of cells in G1 was reduced and a subset of cells with a sub-G1 DNA content accumulated indicative of cells

Figure 1. POT1-loss triggers rapid telomere elongation and a DNA damage response throughout the cell cycle.

A Schematic drawing of the *POT1* gene structure and two derived polypeptides. Exon 6 that has been chosen for gene editing is encircled.

B Schematic drawing of the repair template used for CRISPR/Cas9-mediated gene editing in HEK293E cells. Positions of primers for genotyping PCR are marked with arrows.

C Western blot for POT1 and DDR markers upon *POT1* deletion induced with 0.5 μM 4-OHT. Cl75—parental cell line. gRNA1—POT1 knockout in the population by transient transfection with pSpCas9(BB)-2A-puro containing gRNA1 sequence. EV—corresponding empty vector.

D Time course of telomere length changes upon POT1 removal in clone 35. d (days) TP0—time point 0, no 4OHT.

E Growth curve for *POT1* WT and *POT1* knockout cells. Population doublings (PDL) are represented as mean ± SD (three biological replicates).

F Quantification for TIFs in EdU-positive and EdU-negative cells upon POT1 removal in clone 35. The bars show percentage of cells containing more than 5 TIFs ± SD. Experiments were performed in triplicate. At least 120 cells were analyzed per condition per replicate. Significance was determined using two-way ANOVA. *P*-values are indicated on the graph.

Data information: 4-OHT—4-hydroxytamoxifen, NT—non-treated cells.
Source data are available online for this figure.

 © 2020 The Authors

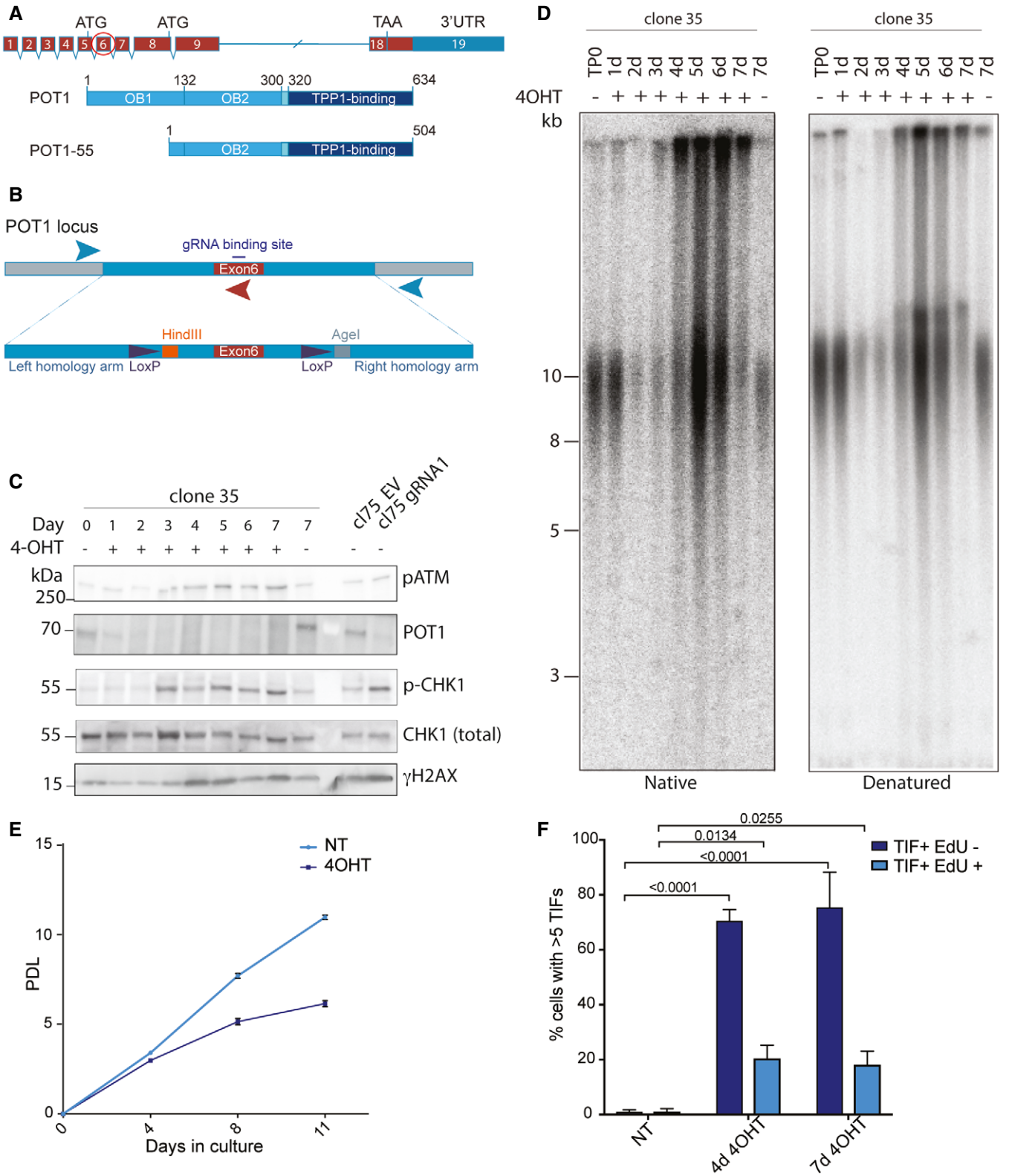

Figure 1.

undergoing cell death by apoptosis. The number of polyploid cells also increased indicating abnormalities in mitosis (Appendix Fig S2A). Immunofluorescence analysis of γ-H2AX foci showed that they colocalized with telomeric DNA, in line with the crucial roles of POT1 in suppressing DNA damage specifically at chromosome ends (Appendix Fig S2B). We pulse-labeled cells with EdU to

© 2020 The Authors

identify cells in S phase. The DNA damage foci were detected in both pulse-labeled EdU-positive and EdU-negative cells (Fig 1F), which lead us to conclude that POT1 suppresses the DNA damage response throughout the cell cycle.

POT1-loss leads to accumulation of single-stranded G-rich DNA, branched DNA structures, and telomere fragility

To test whether the single-stranded G-rich DNA at telomeres was terminal, we treated isolated genomic DNA with commercial 3′–5′ exonuclease I *in vitro* and repeated the native and denatured TRF analysis upon short-term gel electrophoresis which facilitates the quantification of the telomeric signals (Fig 2A). As expected, the G-strand DNA signal on native gels disappeared upon exonuclease I treatment in the uninduced cells containing wild-type POT1 because the signal stems from the telomeric 3′ overhang only (Fig 2A). Upon deletion of *POT1* (lanes labeled with + 4OHT), the native signal was only partially reduced with exonuclease I, indicating that the telomeric DNA accumulated terminal as well as internal single-stranded G-rich DNA in the absence of POT1.

To further characterize the telomeric DNA abnormalities, we used two-dimensional gel electrophoresis (Wang *et al*, 2004). DNA was digested with HinfI and RsaI and electrophoresis in the first and second dimension was performed in the absence and presence of ethidium bromide to estimate DNA size and conformation, respectively (Fig 2B). Telomeric DNA was detected before and after denaturation. In wild-type cells, a single arc was detected consistent with linear double-stranded telomeric DNA with a 3′ overhang (Wang *et al*, 2004). *POT1* deletion led to the appearance of the slow migrating so-called t-complex (Nabetani & Ishikawa, 2009) which was particularly retarded in the presence of ethidium bromide and which therefore is considered to represent branched DNA with double-stranded and single-stranded portions (Nabetani & Ishikawa, 2009). In addition, single-stranded G-rich DNA appeared as an arc, which may stem from unbranched molecules (Fig 2B).

Telomere replication defects lead to accumulation of so-called fragile telomeres in which the telomeric DNA signal detected on metaphase chromosomes is smeared or double (Sfeir *et al*, 2009). We quantified telomere fragility as well as other telomere abnormalities in *POT1* wild-type and knockout cells (Fig 2C and D). We observed a strong increase in telomere fragility from 5 to 10% after 4 days and to 15% after 7 days of *POT1*-deletion. Telomere sister chromatid fusions and chromosome end-to-end fusions also increased but this concerned a much smaller fraction of telomeres (Fig 2D).

Consistent with the analysis by Southern blotting, the metaphase chromosomes of *POT1* knockout cells showed telomere lengthening and a striking increase in telomere length heterogeneity. It is worth noting that telomere fragility was strongly increased already on the day 4 of *POT1* knockout, when telomere length in the knockout cells is very close to the wild type (Appendix Fig S3A). To make sure that increase in telomere fragility was not just a function of telomere length, we used another HEK293E clone, clone 38, that has longer telomeres than clone 35. In this clone, the background fragility was lower than in clone 35, but on day 7 of treatment with 4-OHT the fragility increased twofold, recapitulating the phenotype we describe in clone 35 (Appendix Fig S3B and C).

When observing interphase nuclei, we noticed increased amounts of micronuclei, which is an indication for genomic instability upon POT1-loss (Fig 2E). Finally, while anaphase cells were rare to detect in *POT1* knockout cells, they displayed increased frequency of anaphase bridges, which were likely caused by the chromatid and chromosome fusions (Fig 2E).

The POT1-loss phenotype is caused by deprotection of the G-rich DNA overhang

The POT1 protein contains two OB-folds in its N-terminal half with which it binds single-stranded telomeric DNA (Lei *et al*, 2004). The C-terminal half contains a third split OB-fold which is bound by TPP1 via multiple interactions (Chen *et al*, 2017; Rice *et al*, 2017). For telomere recruitment, the interaction of POT1 with TPP1 is necessary and sufficient (Liu *et al*, 2004; Ye *et al*, 2004; Pinzaru *et al*, 2016). In order to test whether DNA binding by POT1 is required for averting the described telomere abnormalities, we developed a complementation system in which triple HA-tagged POT1 was expressed in the *POT1* knockout cells from a lentiviral construct containing a doxycycline-inducible promoter (Fig 3A). Expression of exogenous POT1 rescued the knockout cells from the DNA damage response and the structural abnormalities in telomeric DNA (Fig 3A and B). Expression of mutant POT1 versions, some of which are associated with cancer development and which in previous analyses showed reduced but not abolished single-stranded DNA binding, could also avert the severe telomere abnormalities when expressed from the plasmid (Fig 3C and D, and Appendix Fig

Figure 2. POT1-loss leads to accumulation of single-stranded G-rich DNA, branched DNA structures, and telomere fragility.

A G-overhang assay for clone 35 upon POT1 removal. The bars show relative amounts of single-stranded telomeric DNA ± SD. Experiments were performed in triplicate.

B 2D gels for telomeric DNA from clone 35 cells with POT1 (NT) and upon POT1 removal for 7 days (7d 4-OHT).

C Examples of metaphase spreads for non-treated (NT) clone 35 cells and clone 35 treated with 4-OHT for 4 and 7 days. White arrowheads indicate fragile telomeres, the red arrowhead indicates a sister chromatid fusion. Scale bar equals 6 μm.

D Quantification of fragile telomeres (left graph), sister chromatid fusions (middle graph), and chromosome fusions (right graph) as a percentage of events per metaphase. Experiments were performed in triplicate. At least 25 metaphases were examined per condition per replicate. The mean is displayed and error bars represent ± SD. Significance was determined using one-way ANOVA. *P*-values are indicated on the graph.

E Quantification and representative images of anaphases with bridges and micronuclei for non-treated (NT) clone 35 cells and clone 35 treated with 4-OHT for 4 and 7 days. Scale bar equals 6 μm. Experiments were performed in triplicate. The bars show percentage of cells containing anaphases, anaphases with bridges, or micronuclei + SD. At least 650 cells were examined per condition per replicate. Significance was determined using one-way ANOVA. *P*-values are indicated on the graph. In all experiments, *POT1* deletion was induced with 0.5 μM 4-OHT.

Data information: 4-OHT—4-hydroxytamoxifen, NT—non-treated cells.
Source data are available online for this figure.

 © 2020 The Authors

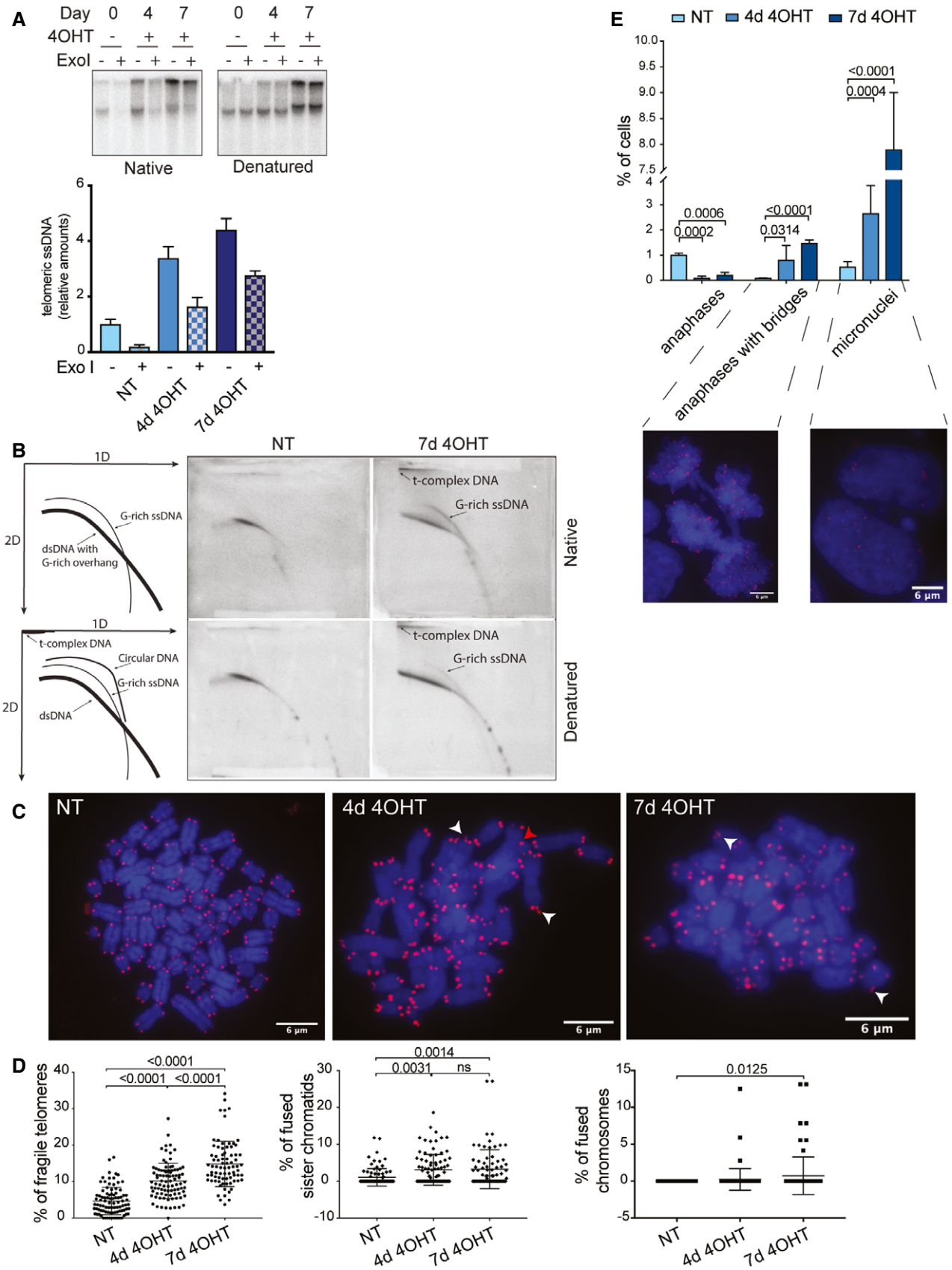
A
Day 0 4 7 0 4 7
4OHT - + + - + +
ExoI - + - + - + - + - + - +
Native
Denatured
telomeric ssDNA (relative amounts)
Exo I - + - + - +
NT
4d 4OHT
7d 4OHT
B
NT
7d 4OHT
1D
2D
G-rich ssDNA
dsDNA with G-rich overhang
t-complex DNA
G-rich ssDNA
Native
Circular DNA
dsDNA
Denatured
C
NT
4d 4OHT
7d 4OHT
6 µm
D
% of fragile telomeres
<0.0001
<0.0001 <0.0001
% of fused sister chromatids
0.0014
0.0031 ns
% of fused chromosomes
0.0125
NT
4d 4OHT
7d 4OHT
E
NT 4d 4OHT 7d 4OHT
% of cells
0.0006
0.0002
<0.0001
0.0314
<0.0001
0.0004
anaphases
anaphases with bridges
micronuclei
6 µm

Figure 2.

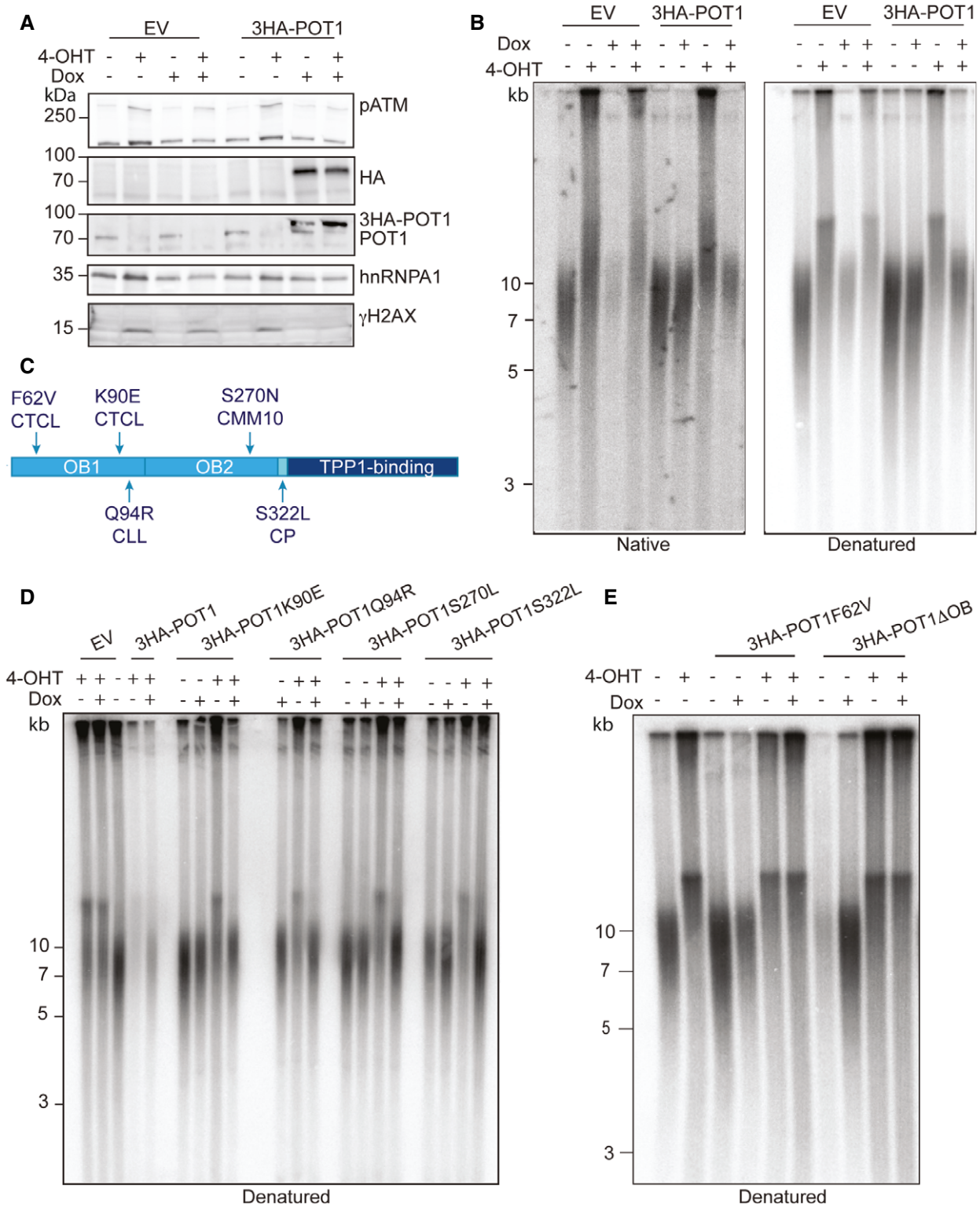

Figure 3. The POT1-loss phenotype is caused by deprotection of the G-rich DNA overhang.

A Western blot for POT1 and DDR markers upon POT1 removal in clone 35 and overexpression of ectopic WT POT1.

B Telomere length and G-overhang length analysis for clone 35 upon POT1 removal and overexpression of ectopic WT POT1 (constant-field gel electrophoresis).

C Schematic of disease-associated mutations in POT1. CTCL—cutaneous T-cell lymphoma, CMM—cutaneous malignant melanoma, CLL—chronic lymphatic leukemia, CP—Coats plus syndrome.

D, E Telomere length and G-overhang length analysis for clone 35 upon POT1 removal and overexpression of ectopic POT1 variants carrying disease-associated mutations (constant-field gel electrophoresis).

© 2020 The Authors

S4A). However, two POT1 mutants were unable to rescue the telomere defects. The POT1F62V point mutation which diminishes single-strand telomeric DNA binding affinity by a factor of 65 (Pinzaru *et al*, 2016), abolished POT1 function with regard to telomeric DNA structure (Fig 3E) as well as suppression of a DNA damage response (Appendix Fig S4B). The same was true for POT1ΔOB lacking the N-terminal OB-fold. Therefore, we conclude that the direct binding of single-stranded telomeric DNA by POT1 is required to prevent telomeric DNA abnormalities. The telomere recruitment via TPP1 is not sufficient for POT1 function.

As our knockout system did not affect a shorter polypeptide derived from the *POT1* locus referred to as POT1-55 (Hockemeyer *et al*, 2005; Fig 1A), we used lentiviral-mediated delivery of shRNA that targets both POT1 forms (Hockemeyer *et al*, 2005) to confirm that the phenotype we observed was POT1-55 independent (Appendix Fig S4C). Indeed, the telomere elongation and DNA damage response phenotypes upon *POT1* knockout induced with 4OHT and POT1 knockdown with shRNA were identical (Appendix Fig S4D).

Development of 2-Step QTIP uncovers substantial remodeling of the telomeric proteome upon POT1-loss

We expected that the above-described telomere abnormalities in the absence of POT1 would trigger substantial changes in the telomeric protein composition. In addition, we considered the possibility that the telomeric DNA abnormalities in *POT1* knockout cells might be caused by inappropriate association of DNA processing enzymes with telomeric DNA in the first place. In order to address these questions, we embarked on isolating and analyzing the telomeric proteome in the presence and absence of POT1. Our laboratory previously developed a quantitative telomeric chromatin isolation protocol (QTIP) in which crosslinked telomeric chromatin is purified with antibodies against the abundant telomere-binding proteins TRF1 and TRF2 and analyzed by mass spectrometry (Grolimund *et al*, 2013; Majerská *et al*, 2017). Different telomeric states were compared by differential SILAC labeling. Here, we wanted to compare telomeric protein composition in a larger set of different samples and therefore opted for the use of tandem mass tag reagents (TMT) (Rauniyar & Yates, 2014; Hogrebe *et al*, 2018; O'Connell *et al*, 2018). In addition, we added to the QTIP method an additional affinity purification step by first purifying the crosslinked and sonicated telomeric chromatin with anti-FLAG sepharose beads containing monoclonal antibodies against the FLAG epitope (Fig 4A). This step became possible as our cell line contained FLAG-tagged TRF1 and TRF2. Immunoprecipitated chromatin was eluted with excess of FLAG peptide and then re-precipitated with polyclonal affinity-purified anti-TRF1 and anti-TRF2 antibodies as in the classical QTIP method. We refer to this method as 2-step QTIP. The two consecutive affinity purification steps yielded a recovery of telomeric DNA of 38–47% and an up to more than 1,000× fold enrichment of telomeric DNA over Alu repeat DNA (Fig 4B).

We performed three biological replicates in uninduced clone 35 cells and cells from which *POT1* had been deleted for 4 or 7 days (Fig 4C). To increase throughput and reduce the analytical variability and the incidence of missing data, we applied a 6-plex TMT isobaric labeling workflow to analyze 2-step QTIP preparations of untreated (NT) and *POT1* knockout cells 4 and 7 days after induced deletion. In addition, we included IgG-negative controls. Each of the three experimental replicates thus constituted a distinct TMT mix. After digestion, labeling, and pooling, peptides in each mix were extensively fractionated by peptide isoelectric focusing to maximize separation and increase depth of protein identification. Spike-in proteins were used to monitor and correct signal levels across replicates and assess the dynamic range of TMT quantitation, which is known to display ratio compression phenomena (Savitski *et al*, 2013; Appendix Fig S5A and B). To maximize sensitivity, we chose not to apply synchronous precursor selection scan methods (McAlister *et al*, 2014). Analysis by mass spectrometry and comparison of 2-step QTIP-purified chromatin to IgG control-purified chromatin indicated that the 2-step QTIP approach yielded telomeric chromatin of unprecedented purity. Indeed, the vast majority of proteins detected were clearly enriched in the QTIP samples compared with the IgG controls (Fig 4C, Table EV1). The 2-step QTIP procedure with fractionation allowed to detect, in addition to the most abundant shelterin components, more than 1,400 proteins. When comparing the telomeric chromatin in wild-type to *POT1* knockout cells, we observed a slight increase in all shelterin components except POT1, which as expected was strongly diminished (Fig 4C). The slight increase of five of the six shelterin proteins can be explained by the telomere elongation that occurred during the experiment (Figs 1D and 2C). 150 proteins were significantly enriched at telomeres that lacked POT1 at day 7 after knockout induction (paired *T*-test with Benjamini–Hochberg FDR correction and threshold at 0.05 on the adjusted *P*-value). Among them, a large set of proteins involved in the DNA damage response and homology-directed DNA repair was identified (Fig 4D).

Figure 4. Development of 2-step QTIP uncovers substantial remodeling of the telomeric proteome upon POT1-loss.

A Schematic drawing of 2-step QTIP (improved version of the quantitative telomeric chromatin isolation protocol (QTIP)).

B Quantification of precipitated telomeric DNA in 2-step QTIP (% of input) and fold enrichment of precipitated telomeric DNA compared with precipitated Alu repeat DNA (based on dot blot analyses). Bars represent data from three independent experiments ± SD.

C Scatter plots representing immunoprecipitation specificity (2-step QTIP/IgG ratio) vs. difference between non-treated cells (NT) and cells at day 4 upon 4-OHT induction (4d 4OHT/NT ratio) or difference between non-treated cells (NT) and cells at day 7 upon 4-OHT induction (7d 4OHT/NT ratio), respectively (data from Table EV1). MRN complex in red, 9-1-1 complex in blue, shelterin complex in orange except for POT1 in black. Values are the average of the 3 biological replicates.

D Heat map representing changes in levels of selected proteins involved in DNA damage (MRN complex in red, 9-1-1 complex in blue) and HDR proteins (purple) after *POT1* knockout induction. Proteins marked with * pass *t*-test, but not *t*-test with Benjamini–Hochberg correction ($P < 0.05$, $q < 0.09$).

Data information: 4-OHT—4-hydroxytamoxifen, NT—non-treated cells.
Source data are available online for this figure.

© 2020 The Authors

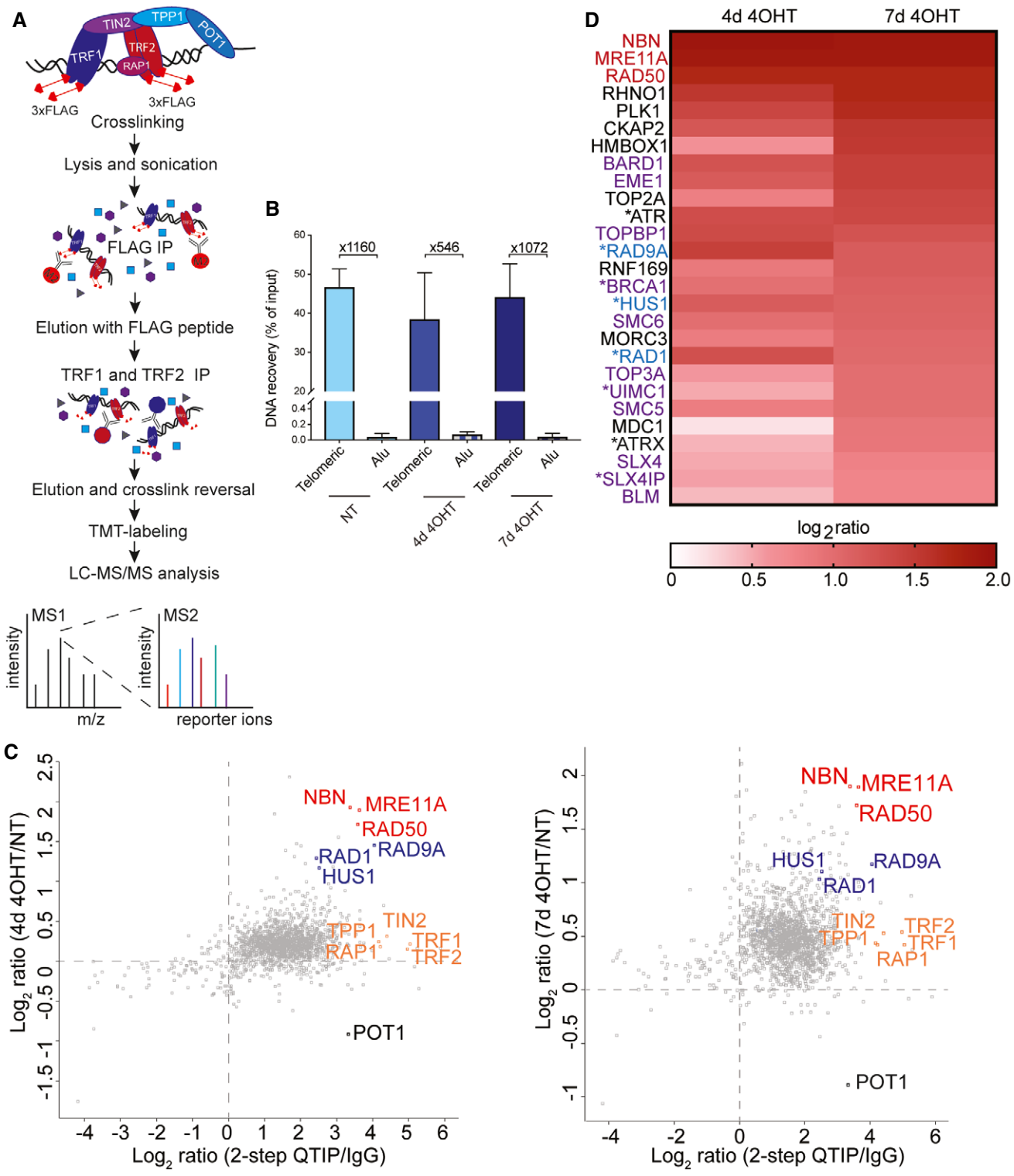

Figure 4.

POT1 prevents telomeric accumulation of homology-directed and other repair factors, nucleases, and cell cycle regulators

We grouped 87 proteins that were significantly enriched at telomeres in *POT1* knockout cells more than 1.5-fold ($\log_2 > 0.6$) into functional classes using the STRING database (Szklarczyk *et al*, 2019). The cutoff chosen takes into consideration TMT ratio compression effects (Appendix Fig S5). Apart from known telomere maintenance components, we identified checkpoint response factors, nucleases, DNA repair proteins, and proteins involved in cell cycle regulation, chromosome organization, centromere function, and RNA metabolism (Fig 5). Interestingly, the largest cluster

© 2020 The Authors

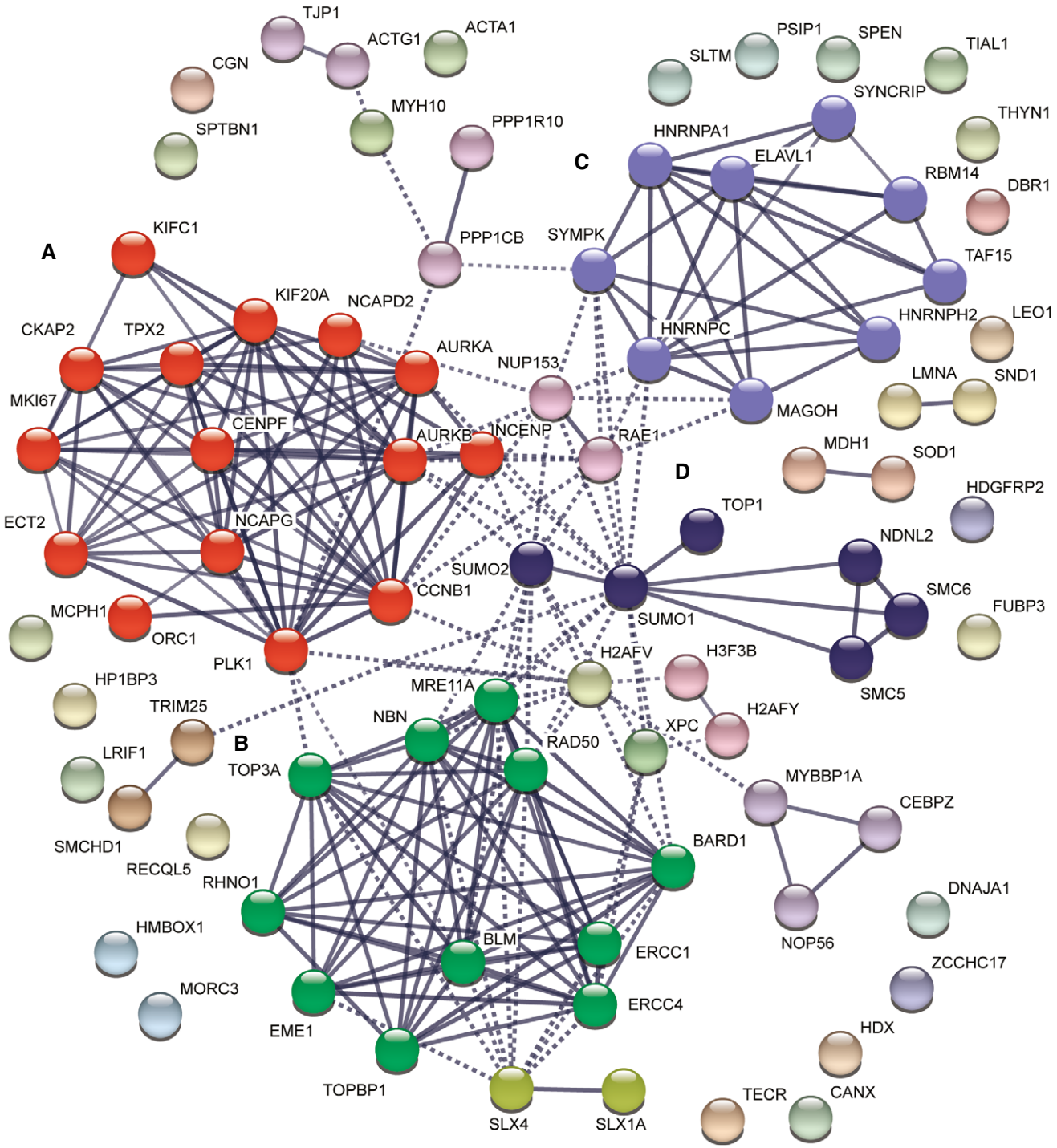

Figure 5. POT1 prevents telomeric accumulation of HDR and other repair factors, nucleases, and cell cycle regulators.

A–D Cluster analysis of proteins enriched at telomeres lacking POT1 using STRING. The largest identified clusters are colored in red (mitosis-associated proteins, (A), green (recombination and DNA damage response proteins, (B), purple (RNA-binding proteins, (C), and dark blue (chromatin and DNA remodelers, (D). Line thickness indicates the strength of data support.

(15 proteins) contained cell cycle and mitosis-associated proteins (Fig 5A). We identified multiple proteins playing roles in spindle formation (AURKA, INCENP, KIFC1, TPX2, AURKB, KIF20A, PLK1). In the same cluster fall two condensin subunits (NCAPD2 and NCAPG) as well as cyclin B1 (CCNB1) and origin recognition complex subunit 1 (ORC1). In the second largest cluster (11 proteins, Fig 5B), we found DNA damage response and repair proteins as well as HR proteins: all components of MRE11/RAD50/NBS1 (MRN) complex, TOPBP1, RHNO1, BARD1, BLM, TOP3A, and the structure-specific endonucleases ERCC1, ERCC4, and EME1.

© 2020 The Authors

SLX4 and SLX1A, which function as Holliday junction resolvases, are also linked to this cluster. Another cluster included proteins involved in RNA metabolism (nine proteins, Fig 5C), which may relate to the increased abundance of R-loops at POT1-depleted telomeres (see below). We also identified a cluster of proteins that contained subunits of the SMC5-SMC6 complex, which is involved in HR as well as TOP1, SUMO1, and SUMO2 (Fig 5D). The latter might stem from sumoylated proteins present at damaged telomeres. Also among proteins enriched at telomeres lacking POT1, we identified SMCHD1 and LRIF1 that have been previously implicated in the telomeric DNA damage response (Vančevska *et al*, 2020), parts of the protein phosphatase 1 complex and lamin A that had been identified at telomeres previously (Kim *et al*, 2009).

Telomere elongation and branching upon POT1-loss is mediated by the HDR machinery

We next embarked on testing whether the identified proteins played roles in establishing or responding to the POT1-loss-mediated phenotype. Since POT1-loss caused telomere elongation, we were particularly intrigued by the enrichment of the HDR factors MRE11, BARD1, BRCA1, and BLM at telomeres. Very strikingly, when we depleted these and other HR factors (RAD51, BRCA1, BRCA2, BARD1, BLM, POLD3) by siRNA in *POT1* knockout cells, telomere elongation, telomere branching, and G-rich single-strand DNA accumulation were all suppressed (Figs 6A, EV1 and EV2, Appendix Fig S6A–D). Incomplete suppression of the phenotype by siRNA knockdown of BLM and POLD3 most probably is due to the incomplete depletion of these proteins. These data therefore indicate that in the absence of POT1 the HDR machinery becomes overly active at telomeres causing severe telomere instability. As POT1 was previously implicated in the regulation of telomerase (Loayza & De Lange, 2003; Kelleher *et al*, 2005; Latrick & Cech, 2010; Zhong *et al*, 2012), we also tested whether telomerase may contribute to the POT1-loss-mediated phenotype adding the telomerase inhibitor GRN163L to cells at the same time when *POT1* deletion was induced (Fig 6B). However, although GRN163L strongly reduced telomerase activity (Appendix Fig S6E), the POT1-loss-mediated phenotype remained unaltered. Thus, telomerase showed no contribution to the phenotype in this experiment. Finally, we tested whether HDR inhibition influenced the DDR observed upon POT1-loss by detecting pCHK1 or γ-H2AX on Western blots (Appendix Fig S6A, Fig EV1B) and by detecting γ-H2AX foci at telomeres by IF-FISH (Appendix Fig S6B). However, in *POT1* knockout cells the DDR still occurred upon suppression of HDR.

POT1-loss leads to accumulation of telomeric R-loops, C-circles, and telomeric PML bodies

Next, we assessed for presence of telomeric DNA-RNA hybrid structures which can be formed with the telomeric long noncoding RNA TERRA and are suppressed at telomeres in wild-type cells by RNA surveillance factors (Azzalin *et al*, 2007; Chawla *et al*, 2011), RNase H (Arora *et al*, 2014; Graf *et al*, 2017), FANCM (Silva *et al*, 2019), and the THO-complex (Pfeiffer *et al*, 2013) but can accumulate in mutant conditions interfering with telomere replication. Strikingly, telomeric R-loops are a hallmark of ALT cells which maintain their telomeres by DNA recombination (Arora *et al*, 2014; Graf *et al*, 2017). To detect telomeric R-loops, the structure-specific antibody S9.6 was used to precipitate from total nucleic acid the R-loops. Telomeric signals in precipitated nucleic acid were quantified by dot blot hybridization (Fig 6C). As a control for the specificity for R-loop precipitation, the nucleic acid samples were treated *in vitro* prior to immunoprecipitation with commercial RNase H. RNase H destroys the RNA moiety in DNA/RNA hybrids. As expected, *in vitro* RNase H treatment abolished the telomeric signal to background levels validating the specificity of the immunoprecipitation for R-loops (Fig 6C). *POT1* deletion caused increased accumulation of telomeric R-loops in the time course experiment. At the same time, *POT1* deletion did not significantly affect TERRA expression levels as detected on Northern blots (Appendix Fig S7A) and it did not significantly affect individual TERRA molecules when the quantities stemming from six different chromosome ends were analyzed by RT–qPCR (Appendix Fig S7B).

Another hallmark of ALT cells is the formation of so-called C-circles which are single-stranded circular DNA molecules containing telomeric C-strand repeats of unknown function (Henson *et al*, 2017). They can be detected by rolling circle amplification followed by hybridization. *POT1* deletion caused a significant increase of C-circles, which however was lower than the amounts detected in U2OS ALT cells (Fig 6D). This increase was partially suppressed by knockdown of BLM (Fig EV1C). ALT cells also demonstrate elevated

Figure 6. Telomere elongation and branching under POT1-loss is mediated by the HDR machinery.

A Telomere length for clone 35 upon POT1 removal and depletion of selected recombination proteins with siRNA (pulsed-field gel electrophoresis).

B Telomere length and G-overhang length analysis for clone 35 upon POT1 removal and inhibition of telomerase with 1 μM GRN163L (pulsed-field gel electrophoresis).

C DRIP assay for DNA-RNA hybrid detection at telomeres in clone 35 upon POT1 removal with S9.6 antibody. Dot blots represent two replicates. Bars represent data from three independent experiments ± SD. The IgG signal was subtracted. Significance was determined using one-way ANOVA, and *P*-values are indicated on the graph.

D C-circle (CC) assay for clone 35 upon POT1 removal. Bars represent data from three independent experiments ± SD. DNA from ALT positive cell line U2OS was used as positive control. Significance was determined using one-way ANOVA, and *P*-values are indicated on the graph. In all experiments, *POT1* deletions were induced with 0.5 μM 4-OHT for 4 and 7 days.

E C-overhang length analysis for clone 35 upon POT1 removal (pulsed-field gel electrophoresis, hybridization with Telo-G probe).

F Quantification and representative pictures for visualization of the PML protein (IF, green) and telomeres (FISH, red) in non-treated (NT) clone 35 cells and clone 35 treated with 4-OHT for 4 and 7 days. Arrows indicate co-localizations. Scale bar equals 10 μm. Bars represent data from three independent experiments ± SD. At least 150 cells were examined per condition per replicate. Significance was determined using one-way ANOVA. *P*-values are indicated on the graph. In all experiments, *POT1* deletion was induced with 0.5 μM 4-OHT.

Data information: 4-OHT—4-hydroxytamoxifen, NT—non-treated cells, GRN163L—telomerase inhibitor Imitelstat, siNT—non-tagreting siRNA, negative control.
Source data are available online for this figure.

 © 2020 The Authors

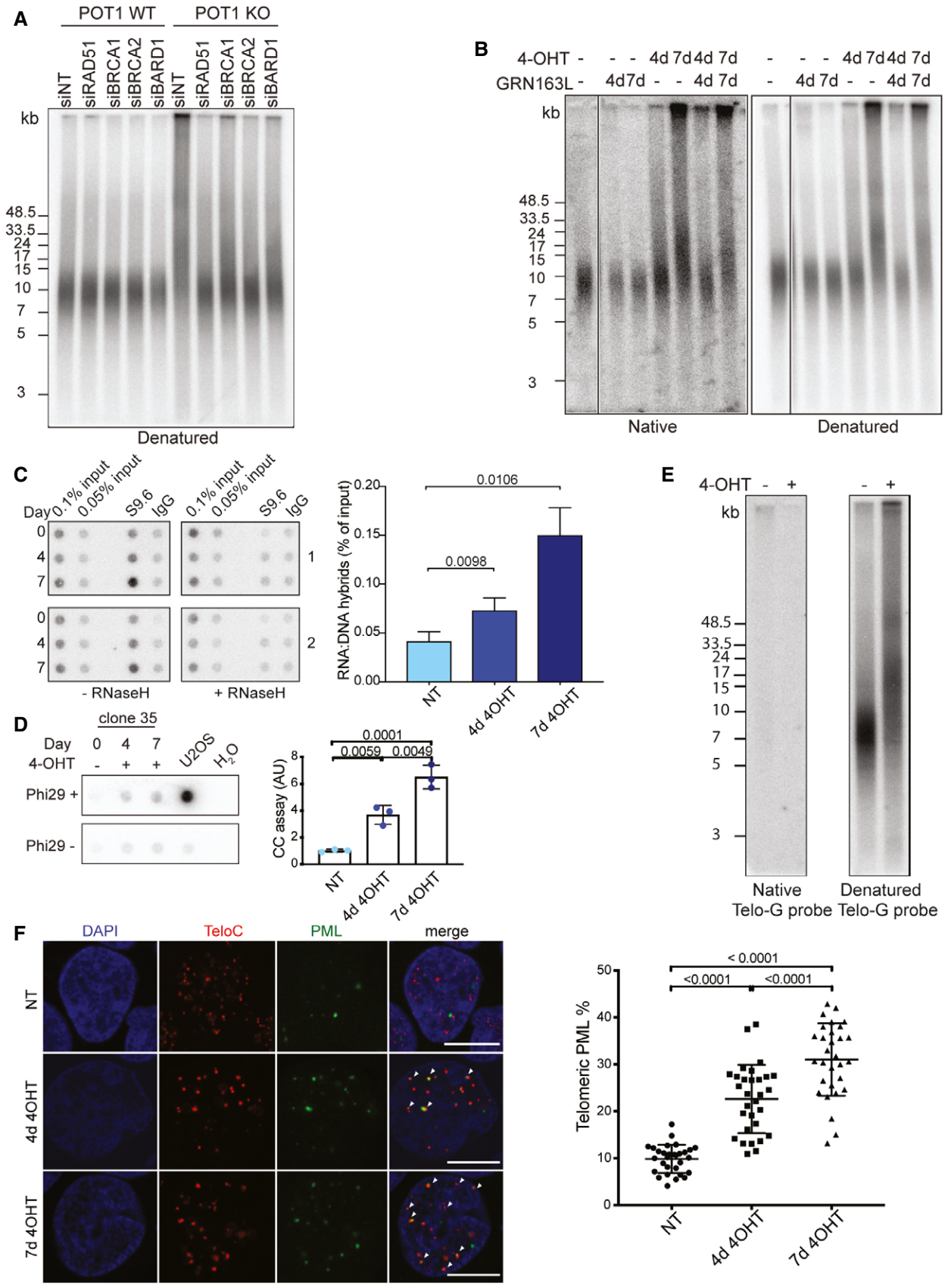
A
POT1 WT
POT1 KO
siNT
siRAD51
siBRCA1
siBRCA2
siBARD1
kb
48.5
33.5
24
17
15
10
7
5
3
Denatured
B
4-OHT
GRN163L
4d 7d
kb
48.5
33.5
24
17
15
10
7
5
3
Native
Denatured
C
Day
0.1% input
0.05% input
S9.6
IgG
- RNaseH
+ RNaseH
RNA:DNA hybrids (% of input)
0.0106
0.0098
NT
4d 4OHT
7d 4OHT
D
clone 35
Day
4-OHT
U2OS
H2O
Phi29 +
Phi29 -
CC assay (AU)
0.0001
0.0059
0.0049
NT
4d 4OHT
7d 4OHT
E
4-OHT
kb
48.5
33.5
24
17
15
10
7
5
3
Native
Telo-G probe
Denatured
Telo-G probe
F
DAPI
TeloC
PML
merge
NT
4d 4OHT
7d 4OHT
Telomeric PML %
< 0.0001
<0.0001
<0.0001
NT
4d 4OHT
7d 4OHT

Figure 6.

levels of C-rich overhangs (Oganesian & Karlseder, 2011). To look at the general changes in the single-stranded C-rich DNA content, we performed in-gel hybridization of non-denatured telomeric DNA with a G-rich telomeric probe (Fig 6E). However, we did not detect any changes of the very week signal observed in wild-type cells.

Finally, we examined the control cells and *POT1* knockout cells for presence of promyelotic leukemia (PML) bodies, which represent another marker for ALT activity (Yeager *et al*, 1999). The percentage of PML foci that were present at telomeres increased upon *POT1* deletion significantly from 10% to more than 30% after 7 days of induced deletion (Fig 6F). Altogether, with increased telomeric R-loops, C-circles and PML bodies the POT1-loss promoted the establishment of three markers that are typical for ALT cells.

POT1 knockout phenotype of HEK293E cells is reproducible in HeLa cells including increase in C-circle formation

Finally, we recapitulated the *POT1*-loss phenotype we observed in 293E cells in the HeLa cell line (Fig EV3). We disrupted the *POT1* genes in HeLa cells with two guiding RNAs and CRISPR/Cas9, causing loss of POT1 protein expression (Fig EV3). POT1-loss caused a rapid increase in telomere length and accumulation of single-stranded branched G-rich DNA (Fig EV3A). We performed a C-circle assay and observed an eightfold increase in C-circle levels, which is comparable to what we detected in 293E cells that had been deleted for *POT1* (Figs 6D and EV3C). This indicates that POT1-loss caused activation of telomeric recombination also in HeLa cells as observed in 293E cells. Interestingly, POT1 depletion with shRNA in HeLa cells was not sufficient to uncover the telomere elongation and DNA damage response phenotypes that were observed upon *POT1* deletion and complete loss of the protein (Fig EV4). Therefore, very low amounts of POT1 are sufficient to prevent the pathological engagement of the recombination machinery with telomeres.

Discussion

Conditional deletion of *POT1* uncovers major roles of this protein in telomere stability

In this paper, we uncover crucial roles of human POT1 in repressing HDR at telomeres which gives rise to severe telomeric DNA abnormalities including telomere elongation, telomere branching, accumulation of single-stranded telomeric DNA, and telomeric R-loops. The establishment of a conditional system and the application of telomere proteomics were crucial to obtain the documented insights. POT1 function had been studied before in several systems but despite its conservation in evolution and the conserved association with G-rich single-stranded telomeric DNA, POT1-loss gave different phenotypes in different model systems. From the work in *Schizosaccharomyces pombe*, POT1 appeared to be most important for the protection of chromosome ends from nucleolytic degradation (Baumann & Cech, 2001). In mice and other rodents, the *POT1* gene is duplicated and different functions have been assigned to the two paralogs indicating remarkable divergence from humans in telomere biology. With mouse cells, the data about a striking function of POT1 paralogs in the suppression of HDR were controversial (Hockemeyer *et al*, 2006; Wu *et al*, 2006), although the data seemed to support subtle contributions in the suppression of HDR at least in mutant backgrounds lacking the Ku end binding protein (Palm *et al*, 2009). In previous depletion studies of human POT1 (Hockemeyer *et al*, 2005; Kim *et al*, 2017), low amounts of POT1 may have been retained being sufficient to efficiently suppress telomeric HDR. Consistently, we also observed in HeLa cells that shRNA-mediated depletion is not efficient enough to unravel the roles of POT1 in suppressing HDR (Figs EV3 and EV4). Residual amounts of POT1 in RNA interference experiments may also explain why the telomeric damage that had been detected by Hockemeyer *et al* (2005) was only prominent in G1, and not in S and G2 phases of the cell cycle, whereas we see DNA damage at telomeres throughout the cell cycle in our system upon *POT1* deletion. From this, one may conclude that absence of POT1 can be tolerated in G1 phase of the cell cycle in immortalized cells and that low levels of POT1 are sufficient at telomeres in S and G2 cells to suppress telomeric HDR that could lead to severe telomere instability, enhanced DNA damage response and possibly, mitotic catastrophe. Also consistent with this notion, we found that POT1 mutants that had been detected in cancer were able to suppress HDR despite the fact that their binding ability of DNA is reduced.

We also observed a significant increase in telomere fragility in the cells lacking POT1 during the time course experiment (Fig 2B, Appendix Fig S3C). Telomere fragility is a hallmark of replication stress (Sfeir *et al*, 2009) and in ALT cells telomere fragility has been suggested to be caused by DNA recombination events among telomeric sequences (Min *et al*, 2017) being consistent with our findings. Interestingly, disease-associated POT1 mutations have been shown to increase telomere fragility and cause replication fork collapse when overexpressed (Pinzaru *et al*, 2016). We suspect that these effects may have been due to slightly increased recombination events at telomeres due to POT1 dysfunction, which may have led to accumulation of recombination by-products and R-loops at telomeres that further challenged replication of telomeric sequences.

In previous work, it has been demonstrated that POT1 can regulate telomerase either negatively or positively (see Introduction). However, we observe that complete absence of human POT1 in HEK293E cells leads to rapid telomere elongation that depends on HDR and does not require telomerase (Figs 6A and B, and EV3C). Thus, our data reveal that POT1 plays crucial roles not only in regulating telomerase but also in suppressing recombination-based mechanisms of telomere elongation. Overall, we suspect that the divergence of observed phenotypes upon POT1 depletion or *POT1* knockout may not reflect fundamental differences in telomere function of POT1 in different model systems. We rather imagine that system-specific variabilities with regard to functional redundancy and abundance of various telomeric proteins may strongly influence the phenotypic outcomes. Whereas POT1 emerges as a master in the protection and regulation of single-strand telomeric DNA, in its absence RPA, CST, RAD51, hnRNPA1, RADX, and telomerase may all compete for binding to the G-rich single-stranded telomeric DNA and guide the faith of chromosome ends toward different outcomes.

2-Step QTIP and TMT labeling unravels the telomeric proteome

We developed and implemented here a 2-step QTIP protocol in order to obtain telomeric chromatin of high purity and TMT

 © 2020 The Authors

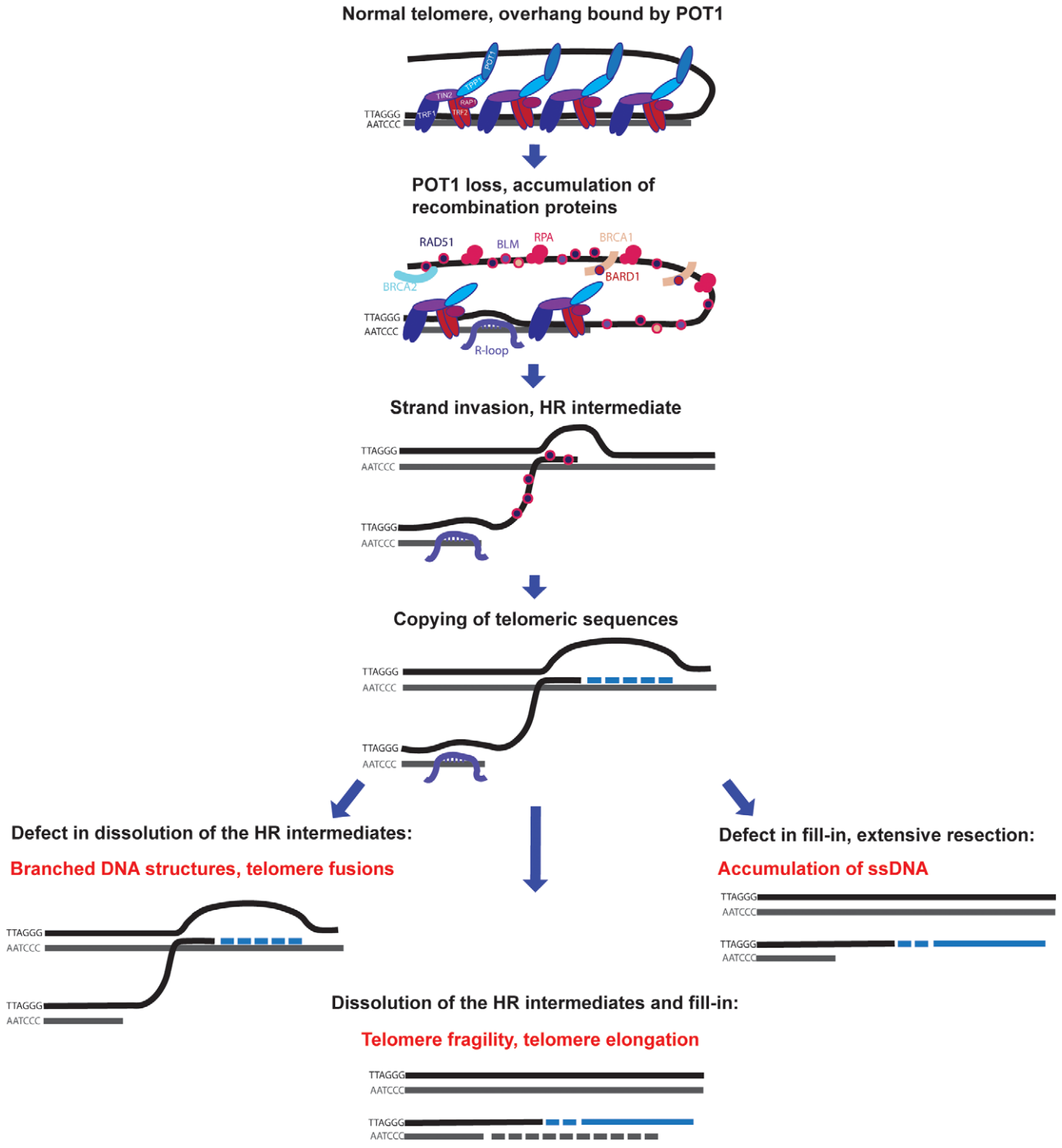

Figure 7. Human POT1 suppresses detrimental HDR.

In the absence of POT1, the telomeric C-strand is resected and RPA and recombination proteins associate with the overhang. RAD51-coated overhangs invade telomeric DNA of adjacent chromosome ends and the invading 3′end is extended by DNA polymerases. Accumulation of R-loops at telomeres facilitates strand invasion. In case of proper dissolution of the HR intermediates, telomeres are elongated and fragility is due to abnormal chromatin condensation after HDR. Defective dissolution of the HR intermediates leads to accumulation of branched DNA structures. Incomplete fill-in synthesis leads to accumulation of G-rich single-stranded DNA.

labeling in order to quantitatively compare the telomeric proteome changes obtained upon POT1-loss. TMT labeling yields highest precision but it suffers from a ratio compression phenomenon and thus underestimates differences in protein abundance (Rauniyar & Yates, 2014; Hogrebe *et al*, 2018; O'Connell *et al*, 2018). Nevertheless, we could identify a large set of proteins whose association

© 2020 The Authors

with telomeres is suppressed by POT1. However, due to variability between biological replicates, several DNA damage proteins that we used as positive controls (for example RAD9A-HUS1-RAD1) did not pass our stringent threshold (paired *t*-test with Benjamini–Hochberg FDR correction and threshold at 0.05 on the adjusted *P*-value) when considering individual subunits. Therefore, we also considered candidates with unadjusted *P*-values < 0.05, especially when all subunits of multiprotein complexes behaved in a consistent manner. As expected for the ATR-dependent DNA damage response, the 9-1-1 complex components and TOPBP1 were enriched at telomeres already at day 4 after induction. Their abundance decreased slightly at day 7 when recombination events became most prevalent. All the other identified DNA damage and HDR proteins were more strongly enriched at telomeres 7 days after induction of *POT1*-deletion. Among the 150 proteins that were significantly enriched, 87 were enriched more than 1.5-fold ($\log_2 > 0.6$) (Fig 5). Apart from the DNA damage proteins whose association was expected, we identified a number of functional protein groups that could not be anticipated. The increased presence of proteins involved in RNA metabolism at POT1-depleted telomeres may be related to the increased amounts of R-loops at telomeres lacking POT1 (Fig 6C). The observed enrichment of mitosis and spindle-associated proteins may stem from the perturbed mitosis in cells lacking POT1 (Fig 2E). The functional relevance of HDR proteins was demonstrated in the current work while for others their exact roles remain to be defined.

Human POT1 suppresses detrimental HDR

Our work supports the following model for human POT1 function (Fig 7). In wild-type cells, the single-stranded telomeric DNA is to a large extent covered by POT1. Upon POT1-loss, the telomeric C-strand is further resected and RPA binds, triggering an ATR dependent checkpoint response. Eventually, RPA is at least partially replaced by RAD51 presumably through BRCA2-mediated loading as during classical recombination. RAD51-coated telomeric 3′ overhangs will invade telomeric DNA of adjacent chromosome ends, which then will be extended by DNA polymerases. The strand invasion is responsible for the observed branched DNA structures. The observed extended 3′ overhangs are due to 3′ end extension upon strand invasion and the presumed 5′ end resection, which follows POT1-loss. In addition, the increased abundance of R-loops between TERRA and the telomeric C-strand should increase single-stranded G-rich telomeric DNA and may facilitate RAD51 binding and telomere recombination (Arora *et al*, 2014; Graf *et al*, 2017). The observed telomere fragility is due to abnormal chromatin condensation following HDR or gaps in telomeric DNA that may remain after the repair process. Overall, our data illustrate that while homology-directed repair is highly beneficial to safeguard the genome from chromosomal breaks, it becomes detrimental when out of check at the natural ends of chromosomes, leading to severe telomere and chromosomal instability. The POT1 protein masters the repression of HDR through its sequence specific DNA binding, covering the single-stranded telomeric DNA. POT1 therefore prevents the unwanted engagement of the HDR repair machinery at telomeres but not elsewhere in the genome.

Materials and Methods

Reagents and Tools table

Reagents and Tools are listed in Table EV2.

Methods and Protocols

Cell lines, CRISPR/Cas9 gene editing, transfections, and lentivirus production

HEK293E cells were grown in DMEM with 10% FCS and penicillin/streptomycin solution (1:100) at 37°C in 5% CO_2. The population doubling (PDL) values were calculated using the mathematical formula PD = [(ln(N2)) − (ln(N1))]/ln(2) where N1 is the number of cells plated and N2 the number of cells harvested.

293E cl75p100 clone was generated from 293E cl75 by transfection of pSpCas9(BB)-2A-GFP (PX458, Ran *et al*, 2013) plasmid expressing gRNA targeting exon 6 of *POT1* (gRNA1, 5′-CAC CGCCCCTGAATCAACTTAAGGG-3′), a recombination reporter plasmid containing a binding site for gRNA1 [pMB1610_pRR-Puro (Flemr & Bühler, 2015)], and pUC19 plasmid containing a repair template for exon 6 of *POT1* (with a modified gRNA-binding site) flanked with LoxP sites and homology arms of 500 bp (pUC19_RT). Cells were selected with 1 μg/ml puromycin for 5 days and clones were isolated by single cell dilution. Clones were screened using 2 genotyping PCRs (with OneTaq polymerase premix from NEB and 1.25 μM primers 1 + 2 and 1 + 3). Positive clones were kept in culture for several weeks to monitor telomere length stability and POT1 levels. The gRNA was designed using http://crispr.mit.edu/ and cloned into pSpCas9(BB)-2A-GFP (PX458).

Cre clones 35, 38, and 45 were generated by transducing cl75p100 cells with lentivirus containing CreERT2, selecting cells with 1 μg/ml puromycin for 5 days, and isolation of clones by single cell dilution. Isolated clones were tested for *POT1* deletion by inducing Cre recombinase with 0.5 μM 4-OHT and clones with the highest recombination efficiency were kept and tested for telomere length stability. Cells were transfected with plasmid DNA using Lipofectamine 2000 (1:200) and 2.5 μg of DNA in 2 ml of OPTIMEM per well in 6-well plates. One day after transfection, cells were split and selected with either puromycin (1 μg/ml) or blasticidin (10 μg/ml). Cells were harvested or diluted 5 days after transfection.

The *POT1* gene was disrupted in HeLa cells by two rounds of Lipofectamine 2000 transfection of pSpCas9(BB)-2A-GFP (PX458, Ran *et al*, 2013) plasmid expressing gRNA targeting exon 6 of *POT1* (gRNA1, 5′-CACCGCCCCTGAATCAACTTAAGGG-3′) and pSpCas9 (BB)-2A-puro (PX459, Ran *et al*, 2013) plasmid expressing gRNA targeting the ATG start codon of *POT1* (gRNA2, 5′-TTCTACAGAAT CAATGTCTT-3′).

Cells were transfected with siRNA pools from Dharmacon using calcium-phosphate transfection with 10 pmol of siRNA in 1 ml of DMEM without antibiotics per well in six well plates. One day after transfection, cells were split and 72 h after transfection cells were harvested for TRF analysis, RT–qPCR, and Western blot analysis.

For lentiviral production, 293T cells were transfected in 10 cm dishes with 4 μg of the corresponding lentiviral vectors (shRNA or transgene) and packaging vectors pMD2.G (1 μg) and pCMVR8.74 (3 μg) using Lipofectamine 2000 (1:400 in OPTIMEM). The next day, the medium was changed for DMEM with 10% FCS and

 © 2020 The Authors

penicillin/streptomycin. The first harvest of viral particles was done 40 h after transfection, and fresh medium was added to the cells. Virus-containing medium was filtered through 0.45 μm filters and 1 ml of filtrate was applied to 1 million of cells in one well of a 6-well plate. The second harvest was done 24 h after the first harvest, and the transduction was repeated as described. The next day, transduced cells were split and selected with puromycin (1 μg/ml), blasticidin (10 μg/ml), or hygromycin (100 μg/ml) for at least 1 week. For doxycycline-inducible expression of POT1, HA-tagged WT *POT1* or mutant *POT1* cDNAs were cloned into pCW22 lentiviral vector between HpaI and PacI restriction sites. Stable cell lines were created by lentiviral transduction and blasticidin selection. Ectopic expression of POT1 constructs was induced with 1 μg/ml doxycycline. For ectopic expression of inducible Cre recombinase, ERT2CreERT2 was subcloned into pLKO1_puro (Stewart *et al*, 2003) digested with PpuMI.

Western blots

1 million cells were resuspended in 100 μl of Laemmli buffer (150 mM Tris–HCl pH 6.8, 4% SDS, 5% beta-mercaptoethanol, 20% glycerol, bromophenol blue) and were boiled for 5 min at 95°C. Equivalents of 100,000 cells were loaded on Mini-PROTEAN TGX™ 4–15% acrylamide gels. Primary antibodies were anti-ATM pS1981 (1:1,000, ab81292; Abcam), anti-γH2AX (1:1,000, 05-636; Millipore), anti-CHK1-pS345 (1:1,000, #2348, Cell signaling), anti-CHK1 (1:1,000, sc-8408, Santa Cruz), anti-RPA32 –S33 (1:1000, A300-246A, Bethyl), anti-vinculin (1:3,000, ab129002, Abcam), and anti-HA (1:3,000, BLG-901502, BioLegend). Secondary antibodies were HRP-conjugated goat anti-mouse (W4021, Promega) and goat anti-rabbit (W4011, Promega). For Western blot analysis of POT1, the membrane was denatured after transfer and re-natured with decreasing concentrations of guanidine-HCl (Wu *et al*, 2007), blocked with 5% milk in TBST and incubated with anti-POT1 (1:1,000, ab124784, Abcam) in 5% milk overnight.

Telomere restriction fragment length analysis and G-overhang assay

Genomic DNA from 3 to 5 million cells was extracted with phenol-chloroform-isoamyl alcohol (25:24:1). 5–10 μg of genomic DNA were digested with 50U HinfI and 30U RsaI in CutSmart buffer (NEB) overnight at 37°C. 3 μg of digested genomic DNA per lane was resolved by pulse field gel electrophoresis in 1% agarose in 0.5× TBE. Samples were electrophoresed for 16 h at 14°C and 5.2 V with 0.5 s initial switch and 6 s final switch using a CHEF-DRII apparatus (Bio-Rad). The gels were dried for 3 h at 50°C, prehybridized with Church buffer (0.5 M Na_2HPO_4 pH 7.2, 1 mM EDTA, 7% SDS, and 1% BSA) and hybridized with a ^{32}P-radiolabeled telomeric probe under native conditions (for G-overhang assay) overnight at 50°C. After hybridization, the gels were washed twice for 30 min with 2× SSC, 0.5%SDS; 1× SSC, 0.25% SDS; 0.5× SSC, 0.1% SDS and 0.5× SSC, and exposed to a phosphorimager screen. Afterward, the gel was denatured (0.5 M NaOH, 1.5 M NaCl), neutralized (0.5 M Tris pH 8.0, 1.5 M NaCl), and re-hybridized as described above. Radioactive signals were detected with Amersham typhoon and quantified in AIDA software version 4.06.034. PRISM7 software was used to calculate relative G-overhang amounts, averages, and *P*-values.

Two-dimensional neutral–neutral agarose gel electrophoresis

Two-dimensional gel electrophoresis was done as described (Wang *et al*, 2004) with modifications. Equal amounts of HinfI+RsaI digested DNA (10–15 μg) were subjected to electrophoresis on 0.4% agarose gels at 30 V for 16 h in the dark at room temperature (first dimension). Then, the lanes were cut and overlaid on top of a second gel (second dimension) containing 1.2% agarose and 0.3 μg/ml ethidium bromide. This gel was run at 4°C and 150 V for 6 h. The gels were processed as described above for the TRF analysis.

Northern blot

10 μg of RNA per lane was loaded on a 1.2% formaldehyde agarose gel and separated by electrophoresis at 100V for 3 h. RNA was transferred to a nylon membrane (Hybond N+) overnight in 1× TBE at 15V. The membrane was UV-crosslinked, prehybridized for 1 h in Church buffer, and hybridized with a ^{32}P-radiolabeled telomeric probe overnight at 55°C. The membrane was washed in 1× SSC, 0.5% SDS twice for 30 min at 60°C and exposed to a phosphorimager screen. Radioactive signals were detected with an Amersham typhoon and quantified in AIDA software version 4.06.034.

Immunofluorescence, click-iT EdU labeling, and telomere fluorescence in situ hybridization (FISH)

Cells were pulse-labeled with 10 μM EdU for 30 min, trypsinized, washed with PBS, and the cell concentration was adjusted to 0.5 million cells in 5% FBS in PBS. 100,000 or 200,000 cells were placed on the microscopic slides using cytospin centrifugation (Shandon cytospin 4; 5 min, 150 g) and were fixed on the slides with 4% paraformaldehyde for 15 min at room temperature. Cells were washed three times with PBS, permeabilized with 0.1% Triton X-100, 0.02% SDS in PBS and stained with azide-coupled fluorophore (Alexa 647) after crosslinking with Click-iT chemistry. Cells were pre-blocked in 2% BSA in PBS, blocked with 10% goat serum in PBS and incubated with anti-γH2AX antibodies (1:1,000). After washing, they were incubated with secondary goat anti-mouse antibodies conjugated with Alexa 488 (1:500). After washes with PBS, cells were incubated in 4% paraformaldehyde for 5 min at room temperature and washed with PBS again and dehydrated with increasing concentrations of ethanol. Cy3-labeled TelC probe (PNA Bio, F1001) was diluted 1:2,000 in hybridization buffer (70% formamide, 10 mM Tris–HCl pH 7.5, 0.5% blocking reagent from Roche) applied on the slides, and slides were denatured for 3 min at 80°C. Slides were then incubated for 3 h in the dark at room temperature, washed twice in hybridization wash buffer 1 (70% formamide, 10 mM Tris–HCl pH 7.5), and washed three times in hybridization buffer 2 (0.1 M Tris–HCl 7.4, 0.15 M NaCl, 0.08% Tween-20). The second wash contained 1 μg/ml DAPI. The slides were mounted with vectashield. Images were taken with a LSM700 upright microscope at 63× magnification. Blinded visual scoring of γH2AX foci colocalizing with telomeric FISH signal in EdU-positive and EdU-negative cells was done using FIJI, and statistical analysis was done using Prism7 software. Normal anaphases, anaphases with bridges, and micronuclei were counted in FIJI, and statistical analysis was done using Prism7 software.

© 2020 The Authors

Telomere fluorescence in situ hybridization (FISH) on metaphase spreads

Cells were treated with 0.5 μg/ml demecolcine for 2 h, harvested with trypsin, incubated with 0.056 M KCl for 7 min at 37°C, fixed with methanol:glacial acetic acid (3:1), and stored overnight at 4°C. Cells were dropped on the microscope slides, dried overnight, and fixed with 4% paraformaldehyde. Telomere FISH was conducted as described above. Images were taken with Zeiss-Axioplan and blinded visual scoring of normal, and aberrant telomeres was done in FIJI. Telomeres were scored as fragile, when the telomeric signals from one chromosome arm was smeared or doubled instead of being a single dot. Single telomeric signal on two corresponding arms of two sister chromatids was scored as sister chromatid fusions. Single telomeric signal between two arms of different chromosomes were scored as chromosome fusions. Statistical analysis was done in Prism7.

RT–qPCR

RNA from 3 million cells was extracted using the Nucleospin RNA extraction kit (Macherey-Nagel). 3 μg of RNA was reverse-transcribed using 200 U super Script III reverse transcriptase (Thermo Fischer), GAPDH, and TERRA reverse primers for 1 h at 55°C, and the reaction was heat inactivated for 15 min at 70°C. 5% of the reaction was used as template for qPCR amplification with Power SYBR Green Master mix (Thermo Fisher) and 0.5 μM forward and reverse primers. The program for qPCR reaction included 10 min at 95°C, 40 cycles at 95°C for 15 s, and 60°C for 1 min in an Applied Biosystems 7900HT Fast Real-Time System (Feretzaki & Lingner, 2017).

RT–qPCR for mRNAs to confirm siRNA-mediated knockdowns was performed using Luna Universal One-Step RT-qPCR Kit (NEB). 200 ng of RNA were used for one-step RT–qPCR with 0.4 μM forward and reverse primers. The program for RT–qPCR included 10 min at 55°C, 1 min at 95°C, followed by 40 cycles at 95°C for 10 s and 60°C for 1 min in an Applied Biosystems 7900HT Fast Real-Time System.

TRAP

TRAP assay was performed as described (Kim, 1997) with modifications. 1 million cells were lysed for 30 min on ice in 200 μl of CHAPS lysis buffer (10 mM Tris–HCl pH 7.5, 1 mM $MgCl_2$, 1 mM EGTA, 0.5% (*w*/*v*) CHAPS, 10% (*w*/*v*) glycerol, 0.1 mM PMSF, 1 mM DTT) and centrifuged for 15 min at 4°C. Lysate concentrations were determined with the Bradford assay and adjusted to 1 μg/μl. Serial dilutions of extracts were used for the primer elongation reaction (1× TRAP buffer, 25 μM dNTPs, 2 ng TS primer, 2 μCi α-^{32}P dGTP (3,000 Ci/mmol) for 30 min at 30°C. Then, telomerase was inactivated at 94°C and 2 U of Taq polymerase (Eurobio) and 2 ng of ACX primers were added to the reaction. PCR included 27 cycles for 30 s at 94°C and 30 s at 60°C. Extracts treated with 0.01 M EDTA were used as negative controls. 20% of TRAP reactions were loaded on 15% non-denaturing polyacrylamide gels and separated at 200 V for 4 h. Gels were dried and exposed to a phosphorimager screen. Radioactive signals were detected with Amersham Typhoon.

DRIP

20 million cells were harvested and each sample was split into two pellets of 10 million cells and lysed on ice with cold RLN buffer (50 mM Tris–HCl, pH 8.0; 140 mM NaCl; 1.5 mM $MgCl_2$; 0.5% *v*/*v* Nonidet P-40; 1 mM DTT; and 100 U/ml RNasin Plus). After centrifugation (300 *g*, 2 min, 4°C), the nuclei-enriched pellets were resuspended in 500 μl of RLT buffer with 0.13% β-mercaptoethanol and homogenized by passing through a 0.9 × 40 mm needle. Nucleic acids were then isolated by a phenol:chloroform:isoamylalcohol (25:24:1; Biosolve BV) extraction, followed by isopropanol precipitation. The two nucleic acid pellets coming from the same sample were joined together and dissolved in 300 μl H_2O. Nucleic acid solutions were sonicated using a Focused-ultrasonicator (Covaris E220) to obtain fragments below 300 bp. 150 μl of sonicated nucleic acids were treated for 90 min at 37°C with either 10 μl of RNase H (1 U/μl; Roche) or H_2O. The reaction was stopped by addition of 2 μl of 0.5 M EDTA. 50% protein G sepharose beads slurry (GE Healthcare Life Sciences) was blocked with 1 mg/ml yeast tRNA for 1 h at 4°C. The samples were then diluted with 1,200 μl of buffer 1 (10 mM Hepes-KOH, pH 7.5; 275 mM NaCl; 0.1% SDS; 1% Triton X-100; and 0.1% Na-deoxycholate) and precleared for 1 h at 4°C. 650 μl of precleared extract were used per immunoprecipitation reaction together with 80 μl of blocked 50% protein G beads slurry, and 1 μg of S9.6 antibody (022715; Kerafast) or mouse IgG (sc-2025; Santa Cruz Biotechnology). The reactions were incubated for 2 h at 4°C on a rotating wheel and then washed consecutively for 5 min each time with 1 ml of buffer 2 (50 mM Hepes-KOH pH 7.5; 140 mM NaCl; 1% Triton X-100; 0.1% Na-deoxycholate; and 1 mM EDTA), buffer 3 (50 mM Hepes-KOH pH 7.5; 500 mM NaCl; 1% Triton X-100; 0.1% Na-deoxycholate; and 1 mM EDTA), buffer 4 (10 mM Tris–HCl pH 8.0; 250 mM LiCl; 1% NP-40; 1% Na-deoxycholate; and 1 mM EDTA), and 1 × TE buffer (10 mM Tris–HCl pH 8.0, and 1 mM EDTA). Beads and inputs were incubated with 1% SDS, 0.1 M $NaHCO_3$, 0.5 mM EDTA pH 8.0, 20 mM Tris–HCl pH 8.0, RNase-DNase free, Roche for 1 h at 65°C and DNA was extracted using the QIAquick PCR purification kit. Samples were transferred to the Hybond N+ membrane using dot bot and UV-crosslinked before hybridization with telomeric probe as described above.

Cell cycle

Cells were incubated with 10 μM EdU for 30 min, harvested, and washed with PBS. Cells were fixed with 70% ethanol at a concentration of 1 million cells per ml. The next day cells were washed with PBS, permeabilized with 0.5% Triton X-100 for 20 min, stained with Alexa-488 conjugated azide using Click-iT chemistry for 30 min in the dark and with 1 μg/ml DAPI, transferred to FACS tubes and cell cycle profiles were acquired with Gallios (Beckman Coulter). Further analysis was done with Kaluza software.

C-circle assay

The C-circle assay was performed as described before (Henson *et al*, 2009). Briefly, 300 ng of genomic DNA was digested with 4 U/μg (each) HinfI and RsaI (NEB) in buffer 2 and 10 μg/ml RNase A for 1 h at 37°C. 30, 10, 3, and 1 ng of digested DNA was taken to perform the φ29 reaction which contained in 20 μl 0.2 mg/ml BSA, 0.1% Tween, 1 mM each of dATP, dGTP, dTTP, 1× φ29 buffer, and 7.5 U φ29 DNA polymerase. The mixture was incubated for 8 h at 30°C, and ϕ29 DNA polymerase was inactivated by incubation at 65°C for 20 min. The reaction products were dot-blotted on a positively charged nylon membrane and UV-crosslinked. The membrane was prehybridized at 50°C for 1 h in Church buffer and hybridized

 © 2020 The Authors

overnight at 50°C with a ^{32}P-radiolabeled telomeric probe. The membrane was washed three times with 4xSSC at RT and once with 4× SSC and 0.1% SDS at 50°C (30 min each wash) and exposed to phosphorimager screen. Radioactive signals were detected with Amersham typhoon and quantified in AIDA software version 4.06.034. Statistical analysis was done using Prism7.

2-step QTIP

Telomeric chromatin precipitation was performed as described before (Majerská *et al* 2017) with a number of modifications. SILAC labeling was not used. One billion cells were used per IP reaction. After harvesting, cells were washed twice with PBS, fixed in 1% formaldehyde and 2 mM EGS for 15 min at 25°C at a cell concentration of 10 million cells/ml. For chromatin enrichment, cells were resuspended in the chromatin enrichment buffer (50 mM Tris–HCl pH 8.0, 1% SDS, 1 mM EDTA) at 10 million cells/ml, incubated on the wheel for 5 min at 25°C, and centrifuged at 2,057 *g* for 5 min. Chromatin enriched pellets were resuspended at 20 million cells/ml in four batches of 25 ml of LB3 buffer (10 mM Tris–HCl, pH 8.0; 200 mM NaCl; 1 mM EDTA–NaOH, pH 8.0; 0.5 mM EGTA–NaOH, pH 8.0; 0.1% *w*/*v* sodium deoxycholate; 0.25% *w*/*v* sodium lauryl sarcosinate; and EDTA-free protease inhibitor complex (Roche)) and sonicated using a Branson Tip sonicator (30% power, 10 s constant pulse, and 20 s pause for a total sonication time of 9 min). Sonicated extracts were dialyzed against immunoprecipitation (IP) buffer (50 mM Tris–HCl pH 8.0, 600 mM NaCl, 10 mM EDTA pH 8, 0.75% Triton X-100) and a first IP was performed using either ANTI-FLAG M2 Affinity Agarose Gel (Sigma) or mouse IgG coupled to sepharose beads that had been blocked with yeast tRNA (1 mg/ml) for 1 h at 4°C. 1.6 ml of 50% beads slurry was used per IP, reactions were performed overnight at 4°C. After five rounds of washes with IP buffer for 5 min each, five rounds of elutions were performed with 100 μg/ml of FLAG peptide (Sigma). A second IP was performed overnight at 4°C with home-made affinity-purified anti-TRF1 and anti-TRF2 antibodies coupled to protein G sepharose beads that had been blocked with yeast tRNA. 0.8 ml of 50% beads slurry was used per IP. After washes with buffer 1 (20 mM Tris–HCl pH 8.0, 0.1% SDS, 1% Triton X-100, 2 mM EDTA pH 8.0, 300 mM NaCl), buffer 2 (20 mM Tris–HCl pH 8.0, 0.1% SDS, 1% Triton, 2 mM EDTA pH 8.0, 500 mM NaCl), buffer 3 (10 mM Tris–HCl pH 8.0, 250 mM LiCl, 1% NP-40, 1% Na-Deoxycholate, 1 mM EDTA pH 8.0) and buffer 4 (10 mM Tris–HCl pH 8.0, 1 mM EDTA pH 8.0), beads were dried and resuspended in 2.5 bed bead volume equivalent of 0.25 M ammonium hydroxide for elution for 15 min at 37°C. Four rounds of elution were performed, and eluates were pooled, flash-frozen, and lyophilized.

Protein digestion

Lyophilized samples were digested following a modified version of the iST method (Kulak *et al*, 2014). Briefly, pellets were resuspended in 100 μl miST lysis buffer (100 mM Tris–HCl pH 8.6, 1% sodium deoxycholate, 10 mM DTT) by vigorous vortexing. An internal standard protein (alcohol dehydrogenase from *Saccharomyces cerevisiae*, Merck-Sigma A7011, 0.02 μg) was spiked in all samples, while 0.05 μg of bovine beta-lactoglobulin (Merck-Sigma L3908) were added only to the TRF1/2 QTIP immunoprecipitates in order to quantify TMT ratio compression effects. Resuspended samples were heated at 95°C for 30 min to denature proteins and reverse formaldehyde-induced crosslinking. Samples were then diluted 1:1 (*v*:*v*) with water containing 4 mM $MgCl_2$ and Benzonase (Merck-Novagen 70746-4, 1:100 of reaction volume = 51.6 Units) and incubated for 1 h at RT to digest nucleic acids crosslinked to proteins. Reduced disulfides were alkylated by adding ¼ vol (50 μl) of 160 mM chloroacetamide (final 32 mM) and incubating at RT for 45 min in the dark. Samples were adjusted to 3 mM EDTA and digested with 1 μg Trypsin/LysC mix (Promega V5073) for 1 h at 37°C, followed by a second overnight digestion with a second, identical aliquot of proteases. To remove sodium deoxycholate, digests were phase extracted by adding 600 μl of ethyl acetate containing 1% TFA, vortexing for 2 min, and centrifugation. The bottom aqueous phase containing peptides was collected, diluted 2× with 0.5% formic acid and desalted on strong cation exchange (SCX) cartridges (SOLA Cartridges (Thermo Fisher: 60209-002)) by centrifugation. After washing the SCX cartridges with 0.5% formic acid, 20% acetonitrile, peptides were eluted in 200 μl of 80% MeCN, 19% water, and 1% (*v*/*v*) ammonia.

An aliquot of 1/15 of samples from experiment replicate 1 (2-2) was analyzed directly by LC-MS and label-free quantitation to assess the quality of the digestion, the specificity of the preparation and, by comparison with known amounts of a standard HeLa digest, obtain an approximate estimate of the total amount (by mass) of peptides present before TMT labeling. The samples appeared to contain approximately 30 μg of material, with antibody chains used for purification seemingly quantitatively dominant, thus making up the bulk of protein material.

TMT labeling

Eluates after SCX desalting were dried, resuspended in 100 μl water, and dried again to remove excess ammonia. Digests were then resuspended in 40 μl of 50 mM TEAB buffer, pH 8.0 and reacted with 0.4 mg of TMT reagent for 1 h at RT, after which excess reagent was quenched with 8 μl of 50% hydroxylamine for 20 min at RT. For each replicate experiment, untreated (NT, day 0) and knockout samples (day 4, day 7) were mixed with their corresponding negative IgG controls in a six-plex TMT experiment using, respectively, TMT channels 126, 127N, 128N, 129N, 130N, and 131. Neutron-encoded C labels were not used). TMT multiplex samples were dried and desalted on C18 SepPak well plates. An aliquot (5%) was injected before fractionation to assess labeling completion (> 98% peptide spectrum matches) by database search with TMT as variable modification (MASCOT software).

Peptide fractionation

Dried desalted eluates were dissolved in 4M urea containing 0.1% ampholytes pH 3–10 (GE Healthcare) and fractionated by off-gel focusing as described (Geiser *et al*, 2011). The 24 peptide fractions obtained were desalted on a SepPak microC18 96-well plate (Waters Corp., Milford, MA), dried, and redissolved in 30 μl of 0.05% trifluroacetic acid, 2% (*v*/*v*) acetonitrile for LC-MS/MS analysis.

MS analysis

Data-dependent LC-MS/MS analysis of extracted peptide mixtures after digestion was carried out on a Fusion Tribrid Orbitrap mass spectrometer (Thermo Fisher Scientific) interfaced through a nano-electrospray ion source to a RSLC 3000 HPLC system (Dionex). Peptides were separated on a reversed-phase custom packed 40 cm

© 2020 The Authors

C18 column (75 μm ID, 100 Å, Reprosil Pur 1.9 μm particles, Dr. Maisch, Germany) with a 4–76% acetonitrile gradient in 0.1% formic acid (total time 140 min). Full MS survey scans were performed at 120,000 resolution. In data-dependent acquisition controlled by Xcalibur 4.0.27 software (Thermo Fisher Scientific), a data-dependent acquisition method was used that optimized the number of precursors selected ("topspeed") of charge 2+ to 5+ while maintaining a fixed scan cycle of 1.5 s. The ion isolation window used was 0.7 Th.

Peptides were fragmented by higher energy collision dissociation (HCD) with a normalized energy of 35%. MS2 scans were done at a resolution of 30,000 in the Orbitrap cell, which is sufficient to resolve 6-plex TMT reporter ions. The m/z of fragmented precursors was then dynamically excluded from selection during 60 s.

MS data analysis

Data files were analyzed with MaxQuant 1.6.3.4 (Cox & Mann, 2008; Cox *et al*, 2011) incorporating the Andromeda search engine (Cox *et al*, 2011). Cysteine carbamidomethylation and TMT labeling (peptide N-termini and lysine side chains) were selected as fixed modification while methionine oxidation and protein N-terminal acetylation were specified as variable modifications. The sequence database used for searching was the human Reference Proteome based on the UNIPROT database (www.uniprot.org), version of October 29th, 2017 (2017_10) containing 71,803 sequences. This was completed with custom databases containing most usual environmental contaminants (keratins, trypsin, etc.), the sequence of yeast ADH, and a collection of mouse (554) and sheep (37) sequences of immunoglobulins (also from UNIPROT). Mass tolerance was 4.5 ppm on precursors (after recalibration) and 20 ppm on HCD fragments. Both peptide and protein identifications were filtered at 1% FDR relative to hits against a decoy database built by reversing protein sequences. For unlabeled samples, iBAQ values (Schwanhäusser *et al*, 2011) generated by MaxQuant in label-free quantitation were used. For TMT analysis, the raw reporter ion intensities generated by MaxQuant and summed for each protein group were used in all following steps to derive quantitation. Only identified peptide ions with a precursor intensity fraction (PIF parameter) greater than 0.75 were accepted and used for TMT quantitation.

Processing of quantitative data and statistical tests

The MaxQuant output table "proteinGroups.txt" for the three TMT replicate samples was first processed to remove proteins matched to the contaminant database as well as proteins identified only by modified peptides and reverse database hits, yielding a first unfiltered list of 2,674 identified proteins. As the composition of positive and negative samples was very different, no global normalization was applied to the data. After log-2 transformation of all intensity values, a plot of the intensity of the spiked-in control (yeast ADH) showed a slight decrease of signal intensity correlating with the order of MS injection (Appendix Fig S5). A global correction factor was applied per TMT sample mix to compensate for this effect, which is probably in partly due to gradual deterioration of the performance of the LC column over the > 80 h of continuous MS measurement. The largest correction factor was +0.28 ($\log_2$ scale) relative to the median of all samples. Next, the table was filtered to retain only proteins identified by a minimum of two "razor or unique" peptides and having at least 12 out of 18 total quantitative values (1,695 proteins left). Ratios (difference in log scale) were calculated for each sample relative to its IgG control.

A one-sample t-test (P-value filter at 0.05) was performed on all values by comparing the 9 TRF1/2 IP's vs. 9 IgG controls to identify a set of invariant proteins that did not significantly change in intensity between IgG controls and positive IP's. 249 proteins (including many keratins and common contaminants) passed the test and were removed from the dataset, leaving 1,446 protein groups. The obtained ratio QTIP/IgG was recorded in the tables as "specificity ratio". To determine proteins significantly changing between NT and the knockout (day 4, day 7) conditions, we applied a paired t-test (each sample against its IgG control) with Benjamini–Hochberg FDR correction (Benjamini & Hochberg, 1995) and threshold at 0.05 on the adjusted P-value. No protein passed the test at day 4 while 150 proteins passed the test at day 7. Analysis was performed using Perseus (Tyanova *et al*, 2016).

Data availability

All raw MS data together with MaxQuant output tables are available via the ProteomXchange data repository (https://www.ebi.ac.uk/pride/archive) with the accession number PXD016826.

Expanded View for this article is available online.

Acknowledgements

We thank members of the Lingner laboratory for fruitful discussions, the Protein Expression Core Facility at EPFL for 293E cells, Gérald Lossaint for 293E cl75, Pierre Gönzy for U2OS cells, Etienne Meylan for the pCW22 construct and Jerry Shay (UT Southwestern) for GRN163L. Research in J.L.'s laboratory was supported by the Swiss National Science Foundation (SNSF grant 310030_184718), the SNSF funded NCCR RNA and disease network (grant 182880), an Initial Training Network (ITN) grant (aDDRess) from the European Commission's Seventh Framework Programme (grant No 812829), the Swiss Cancer League (KLS-3824-02-2016) and EPFL.

Author contributions

GG carried out all experiments except for the mass spectrometry analysis, which was done by MQ. A-SB carried out initial experiments demonstrating that RAD51 depletion rescues from telomeric DNA abnormalities observed in *POT1* knockout cells. GG and JL wrote the paper. The study was conceptualized by GG and JL.

Conflict of interest

The authors declare that they have no conflict of interest.

References

Arora R, Lee Y, Wischnewski H, Brun CM, Schwarz T, Azzalin CM (2014) RNaseH1 regulates TERRA-telomeric DNA hybrids and telomere maintenance in ALT tumour cells. *Nat Commun* 5: 5220

Azzalin CM, Reichenbach P, Khoriauli L, Giulotto E, Lingner J (2007) Telomeric repeat containing RNA and RNA surveillance factors at mammalian chromosome ends. *Science* 318: 798 – 801

Baumann P, Cech TR (2001) Pot1, the putative telomere end-binding protein in fission yeast and humans. *Science* 292: 1171 – 1175

 © 2020 The Authors

Benjamini Y, Hochberg Y (1995) Controlling the false discovery rate: a practical and powerful approach to multiple testing. *J R Stat Soc B (Methodol)* 57: 289 – 300

Chawla R, Redon S, Raftopoulou C, Wischnewski H, Gagos S, Azzalin CM (2011) Human UPF1 interacts with TPP1 and telomerase and sustains telomere leading-strand replication. *EMBO J* 30: 4047 – 4058

Chen C, Gu P, Wu J, Chen X, Niu S, Sun H, Wu L, Li N, Peng J, Shi S *et al* (2017) Structural insights into POT1-TPP1 interaction and POT1 C-terminal mutations in human cancer. *Nat Commun* 8: 14929

Cox J, Mann M (2008) MaxQuant enables high peptide identification rates, individualized p.p.b.-range mass accuracies and proteome-wide protein quantification. *Nat Biotechnol* 26: 1367 – 1372

Cox J, Michalski A, Mann M (2011) Software lock mass by two-dimensional minimization of peptide mass errors. *J Am Soc Mass Spectrom* 22: 1373 – 1380

Doksani Y, Wu JY, de Lange T, Zhuang X (2013) Super-resolution fluorescence imaging of telomeres reveals TRF2-dependent T-loop formation. *Cell* 155: 345 – 356

Feretzaki M, Lingner J (2017) A practical qPCR approach to detect TERRA, the elusive telomeric repeat-containing RNA. *Methods* 114: 39 – 45

Flemr M, Bühler M (2015) Single-step generation of conditional knockout mouse embryonic stem cells. *Cell Rep* 12: 709 – 716

Geiser L, Dayon L, Vaezzadeh AR, Hochstrasser DF (2011) Shotgun proteomics: a relative quantitative approach using Off-Gel electrophoresis and LC-MS/MS. *Methods Mol Biol* 681: 459 – 472

Graf M, Bonetti D, Lockhart A, Serhal K, Kellner V, Maicher A, Jolivet P, Teixeira MT, Luke B (2017) Telomere length determines TERRA and R-loop regulation through the cell cycle. *Cell* 170: 72 – 85.e14

Grolimund L, Aeby E, Hamelin R, Armand F, Chiappe D, Moniatte M, Lingner J (2013) A quantitative telomeric chromatin isolation protocol identifies different telomeric states. *Nat Commun* 4: 2848

Henson JD, Cao Y, Huschtscha LI, Chang AC, Au AYM, Pickett HA, Reddel RR (2009) DNA C-circles are specific and quantifiable markers of alternative-lengthening-of-telomeres activity. *Nat Biotechnol* 27: 1181 – 1185

Henson JD, Lau LM, Koch S, Martin La Rotta N, Dagg RA, Reddel RR (2017) The C-Circle Assay for alternative-lengthening-of-telomeres activity. *Methods* 114: 74 – 84

Hockemeyer D, Sfeir AJ, Shay JW, Wright WE, de Lange T (2005) POT1 protects telomeres from a transient DNA damage response and determines how human chromosomes end. *EMBO J* 24: 2667 – 2678

Hockemeyer D, Daniels J-P, Takai H, de Lange T (2006) Recent expansion of the telomeric complex in rodents: two distinct POT1 proteins protect mouse telomeres. *Cell* 126: 63 – 77

Hogrebe A, von Stechow L, Bekker-Jensen DB, Weinert BT, Kelstrup CD, Olsen JV (2018) Benchmarking common quantification strategies for large-scale phosphoproteomics. *Nat Commun* 9: 1045

Kelleher C, Kurth I, Lingner J (2005) Human protection of telomeres 1 (POT1) is a negative regulator of telomerase activity *in vitro*. *Mol Cell Biol* 25: 808 – 818

Kim N (1997) Advances in quantification and characterization of telomerase activity by the telomeric repeat amplification protocol (TRAP). *Nucleic Acids Res* 25: 2595 – 2597

Kim H, Lee O-H, Xin H, Chen L-Y, Qin J, Chae HK, Lin S-Y, Safari A, Liu D, Songyang Z (2009) TRF2 functions as a protein hub and regulates telomere maintenance by recognizing specific peptide motifs. *Nat Struct Mol Biol* 16: 372 – 379

Kim H, Li F, He Q, Deng T, Xu J, Jin F, Coarfa C, Putluri N, Liu D, Songyang Z (2017) Systematic analysis of human telomeric dysfunction using inducible telosome/shelterin CRISPR/Cas9 knockout cells. *Cell Discov* 3: 17034

Kulak NA, Pichler G, Paron I, Nagaraj N, Mann M (2014) Minimal, encapsulated proteomic-sample processing applied to copy-number estimation in eukaryotic cells. *Nat Methods* 11: 319 – 324

de Lange T (2018) Shelterin-mediated telomere protection. *Annu Rev Genet* 52: 223 – 247

Latrick CM, Cech TR (2010) POT1-TPP1 enhances telomerase processivity by slowing primer dissociation and aiding translocation. *EMBO J* 29: 924 – 933

Lazzerini-Denchi E, Sfeir A (2016) Stop pulling my strings – what telomeres taught us about the DNA damage response. *Nat Rev Mol Cell Biol* 17: 364 – 378

Lei M, Podell ER, Cech TR (2004) Structure of human POT1 bound to telomeric single-stranded DNA provides a model for chromosome end-protection. *Nat Struct Mol Biol* 11: 1223 – 1229

Lin Y-C, Boone M, Meuris L, Lemmens I, Van Roy N, Soete A, Reumers J, Moisse M, Plaisance S, Drmanac R *et al* (2014) Genome dynamics of the human embryonic kidney 293 lineage in response to cell biology manipulations. *Nat Commun* 5: 4767

Lin C-YG, Näger A-C, Lunardi T, Vančevska A, Lossaint G, Lingner J (2020) The human telomeric proteome during telomere replication. *bioRxiv* https://doi.org/10.1101/2020.06.14.150524 [PREPRINT]

Liu D, O'Connor MS, Qin J, Songyang Z (2004) Telosome, a mammalian telomere-associated complex formed by multiple telomeric proteins. *J Biol Chem* 279: 51338 – 51342

Loayza D, De Lange T (2003) POT1 as a terminal transducer of TRF1 telomere length control. *Nature* 423: 1013 – 1018

Majerská J, Redon S, Lingner J (2017) Quantitative telomeric chromatin isolation protocol for human cells. *Methods* 114: 28 – 38

McAlister GC, Nusinow DP, Jedrychowski MP, Wühr M, Huttlin EL, Erickson BK, Rad R, Haas W, Gygi SP (2014) MultiNotch MS3 enables accurate, sensitive, and multiplexed detection of differential expression across cancer cell line proteomes. *Anal Chem* 86: 7150 – 7158

Min J, Wright WE, Shay JW (2017) Alternative lengthening of telomeres mediated by mitotic DNA synthesis engages break-induced replication processes. *Mol Cell Biol* 37: e00226-17

Miyoshi T, Kanoh J, Saito M, Ishikawa F (2008) Fission yeast Pot1-Tpp1 protects telomeres and regulates telomere length. *Science* 320: 1341 – 1344

Nabetani A, Ishikawa F (2009) Unusual telomeric DNAs in human telomerase-negative immortalized cells. *Mol Cell Biol* 29: 703 – 713

O'Connell JD, Paulo JA, O'Brien JJ, Gygi SP (2018) Proteome-wide evaluation of two common protein quantification methods. *J Proteome Res* 17: 1934 – 1942

Oganesian L, Karlseder J (2011) Mammalian 5′ C-rich telomeric overhangs are a mark of recombination-dependent telomere maintenance. *Mol Cell* 42: 224 – 236

Palm W, Hockemeyer D, Kibe T, de Lange T (2009) Functional dissection of human and mouse POT1 proteins. *Mol Cell Biol* 29: 471 – 482

Pfeiffer V, Crittin J, Grolimund L, Lingner J (2013) The THO complex component Thp2 counteracts telomeric R-loops and telomere shortening. *EMBO J* 32: 2861 – 2871

Pinzaru AM, Hom RA, Beal A, Phillips AF, Ni E, Cardozo T, Nair N, Choi J, Wuttke DS, Sfeir A *et al* (2016) Telomere replication stress induced by POT1 inactivation accelerates tumorigenesis. *Cell Rep* 15: 2170 – 2184

Pitt CW, Cooper JP (2010) Pot1 inactivation leads to rampant telomere resection and loss in one cell cycle. *Nucleic Acids Res* 38: 6968 – 6975

Ran FA, Hsu PD, Wright J, Agarwala V, Scott DA, Zhang F (2013) Genome engineering using the CRISPR-Cas9 system. *Nat Protoc* 8: 2281 – 2308

Rauniyar N, Yates JR (2014) Isobaric labeling-based relative quantification in shotgun proteomics. *J Proteome Res* 13: 5293 – 5309

© 2020 The Authors

Rice C, Shastrula PK, Kossenkov AV, Hills R, Baird DM, Showe LC, Doukov T, Janicki S, Skordalakes E (2017) Structural and functional analysis of the human POT1-TPP1 telomeric complex. *Nat Commun* 8: 14928

Savitski MM, Mathieson T, Zinn N, Sweetman G, Doce C, Becher I, Pachl F, Kuster B, Bantscheff M (2013) Measuring and managing ratio compression for accurate iTRAQ/TMT quantification. *J Proteome Res* 12: 3586 – 3598

Schindelin J, Arganda-Carreras I, Frise E, Kaynig V, Longair M, Pietzsch T, Preibisch S, Rueden C, Saalfeld S, Schmid B *et al* (2012) Fiji: an open-source platform for biological-image analysis. *Nat Methods* 9: 676 – 682

Schwanhäusser B, Busse D, Li N, Dittmar G, Schuchhardt J, Wolf J, Chen W, Selbach M (2011) Global quantification of mammalian gene expression control. *Nature* 473: 337 – 342

Sfeir A, Kosiyatrakul ST, Hockemeyer D, MacRae SL, Karlseder J, Schildkraut CL, de Lange T (2009) Mammalian telomeres resemble fragile sites and require TRF1 for efficient replication. *Cell* 138: 90 – 103

Silva B, Pentz R, Figueira AM, Arora R, Lee YW, Hodson C, Wischnewski H, Deans AJ, Azzalin CM (2019) FANCM limits ALT activity by restricting telomeric replication stress induced by deregulated BLM and R-loops. *Nat Commun* 10: 2253

Stewart SA, Dykxhoorn DM, Palliser D, Mizuno H, Yu EY, An DS, Sabatini DM, Chen IS, Hahn WC, Sharp PA, *et al* (2003) Lentivirus-delivered stable gene silencing by RNAi in primary cells. *RNA* 9: 493 – 501

Szklarczyk D, Gable AL, Lyon D, Junge A, Wyder S, Huerta-Cepas J, Simonovic M, Doncheva NT, Morris JH, Bork P *et al* (2019) STRING v11: protein–protein association networks with increased coverage, supporting functional discovery in genome-wide experimental datasets. *Nucleic Acids Res* 47: D607 – D613

Takai KK, Kibe T, Donigian JR, Frescas D, de Lange T (2011) Telomere protection by TPP1/POT1 requires tethering to TIN2. *Mol Cell* 44: 647 – 659

Tyanova S, Temu T, Sinitcyn P, Carlson A, Hein MY, Geiger T, Mann M, Cox J (2016) The Perseus computational platform for comprehensive analysis of (prote)omics data. *Nat Methods* 13: 731 – 740

Vančevska A, Pfeiffer V, Feretzaki M, Ahmed W, Lingner J (2020) SMCHD1 promotes ATM-dependent DNA damage signaling and repair of uncapped telomeres. *EMBO J* 39: e102668

Wang RC, Smogorzewska A, de Lange T (2004) Homologous recombination generates T-loop-sized deletions at human telomeres. *Cell* 119: 355 – 368

Wu L, Multani AS, He H, Cosme-Blanco W, Deng Y, Deng JM, Bachilo O, Pathak S, Tahara H, Bailey SM *et al* (2006) Pot1 deficiency initiates DNA damage checkpoint activation and aberrant homologous recombination at telomeres. *Cell* 126: 49 – 62

Wu Y, Li Q, Chen X-Z (2007) Detecting protein–protein interactions by far western blotting. *Nat Protoc* 2: 3278 – 3284

Ye JZ-S, Donigian JR, van Overbeek M, Loayza D, Luo Y, Krutchinsky AN, Chait BT, de Lange T (2004) TIN2 binds TRF1 and TRF2 simultaneously and stabilizes the TRF2 complex on telomeres. *J Biol Chem* 279: 47264 – 47271

Yeager TR, Neumann AA, Englezou A, Huschtscha LI, Noble JR, Reddel RR (1999) Telomerase-negative immortalized human cells contain a novel type of promyelocytic leukemia (PML) body. *Cancer Res* 59: 4175 – 4179

Zhong FL, Batista LFZ, Freund A, Pech MF, Venteicher AS, Artandi SE (2012) TPP1 OB-fold domain controls telomere maintenance by recruiting telomerase to chromosome ends. *Cell* 150: 481 – 494

 © 2020 The Authors